The Astrophysical Journal, 782:84 (20pp), 2014 February 20 doi:10.1088/0004-637X/782/2/84

COSMOLOGICAL ZOOM SIMULATIONS OF $z = 2$ GALAXIES: THE IMPACT OF GALACTIC OUTFLOWS

Daniel Anglés-Alcázar[1], Romeel Davé[2,3,4,5], Feryal Özel[2,6], and Benjamin D. Oppenheimer[7]
[1] Department of Physics, University of Arizona, Tucson, AZ 85721, USA; anglesd@email.arizona.edu
[2] Department of Astronomy, University of Arizona, Tucson, AZ 85721, USA
[3] University of the Western Cape, Bellville, Cape Town 7535, South Africa
[4] South African Astronomical Observatories, Observatory, Cape Town 7525, South Africa
[5] African Institute for Mathematical Sciences, Muizenberg, Cape Town 7545, South Africa
[6] Radcliffe Institute for Advanced Study, Harvard University, Cambridge, MA 02138, USA
[7] Leiden Observatory, Leiden University, P.O. Box 9513, 2300 RA Leiden, The Netherlands
Received 2013 May 1; accepted 2013 November 24; published 2014 January 31

ABSTRACT

We use high-resolution cosmological zoom simulations with ∼200 pc resolution at $z = 2$ and various prescriptions for galactic outflows in order to explore the impact of winds on the morphological, dynamical, and structural properties of eight individual galaxies with halo masses $\sim 10^{11}$–2×10^{12} $M_\odot$ at $z = 2$. We present a detailed comparison to spatially and spectrally resolved $H\alpha$ and other observations of $z \approx 2$ galaxies. We find that simulations without winds produce massive, compact galaxies with low gas fractions, super-solar metallicities, high bulge fractions, and much of the star formation concentrated within the inner kiloparsec. Strong winds are required to maintain high gas fractions, redistribute star-forming gas over larger scales, and increase the velocity dispersion of simulated galaxies, more in agreement with the large, extended, turbulent disks typical of high-redshift star-forming galaxies. Winds also suppress early star formation to produce high-redshift cosmic star formation efficiencies in better agreement with observations. Sizes, rotation velocities, and velocity dispersions all scale with stellar mass in accord with observations. Our simulations produce a diversity of morphological characteristics—among our three most massive galaxies, we find a quiescent grand-design spiral, a very compact star-forming galaxy, and a clumpy disk undergoing a minor merger; the clumps are evident in Hα but not in the stars. Rotation curves are generally slowly rising, particularly when calculated using azimuthal velocities rather than enclosed mass. Our results are broadly resolution-converged. These results show that cosmological simulations including outflows can produce disk galaxies similar to those observed during the peak epoch of cosmic galaxy growth.

Key words: galaxies: evolution – galaxies: formation – galaxies: high-redshift – galaxies: kinematics and dynamics – galaxies: structure

Online-only material: color figures

1. INTRODUCTION

The epoch around redshift $z \sim 2$ is the most active period of cosmic star formation (Madau et al. 1996; Hopkins & Beacom 2006), and appears to be the period when the familiar Hubble sequence first began to emerge. It is thus a critical epoch for understanding how galaxies form, grow, and evolve into the populations we see today. The advent of near-infrared integral field spectrometers on 8–10 m class ground-based telescopes has enabled spatially and spectrally resolved observations of an increasing number of galaxies at this epoch (e.g., Förster Schreiber et al. 2006, 2009; Cresci et al. 2009; Law et al. 2009; Wright et al. 2009; Alaghband-Zadeh et al. 2012; Swinbank et al. 2012b). These studies are complemented by space-based observations with the *Hubble Space Telescope*, enabling a detailed study of the distributions of star formation and stellar populations (e.g., Elmegreen et al. 2004, 2009; Wuyts et al. 2012), and *Spitzer* and *Herschel*, providing infrared data that better constrains the total stellar mass and bolometric emission of these galaxies (e.g., Nordon et al. 2010; Rodighiero et al. 2010; Wuyts et al. 2011). Such data are providing a comprehensive view of the structure, kinematics, and star formation properties of galaxies at early stages of their evolution.

These observations provide new and unexplored avenues with which to constrain models of galaxy formation and evolution. In particular, the resolved (both spatially and spectrally) information that is now available provides detailed constraints on the assembly of galaxies at $z \sim 2$. The galaxy population at this epoch displays a remarkable level of diversity, with many properties unlike anything seen locally, from extremely compact and (relatively) quiescent ellipticals (van Dokkum et al. 2008; Barro et al. 2013), to extended turbulent and clumpy disks (Förster Schreiber et al. 2009; Genzel et al. 2011), to galaxies forming stars at hundreds to thousands of solar masses per year (Chapman et al. 2010; Alaghband-Zadeh et al. 2012; Targett et al. 2013). Capturing this diversity, both qualitatively and quantitatively, presents an enormous challenge for galaxy formation models, one that is only now beginning to be addressed using the latest computational tools.

Cosmological hydrodynamic simulations have now matured to the point that they yield galaxy populations broadly in agreement with observations across a range of redshifts (e.g., Davé et al. 2011b, 2011a; McCarthy et al. 2012; Torrey et al. 2013; Kannan et al. 2013). While there are still many discrepancies with even the latest models (e.g., Weinmann et al. 2012), overall it appears that the galaxy population is in general agreement with expectations from a Λ cold dark matter (ΛCDM) cosmology, combined with numerous feedback mechanisms from star formation, photo-ionizing radiation, and active galactic nuclei that help establish the properties of galaxies assembling within hierarchically growing halos. The emerging paradigm is that galaxy evolution at this epoch is governed by a balance between inflows from the intergalactic medium (IGM) and powerful, ubiquitous outflows that intimately connect galaxies and their

surroundings in a "baryon cycle" of exchanging mass, energy, and metals (e.g., Davé et al. 2012; Lilly et al. 2013).

Resolved studies of distant galaxies present a new challenge to such models. In order to meet this challenge, numericists have begun to employ the "zoom" technique to expand the dynamic range sufficiently to model such observations. In zoom simulations, a sub-volume extracted from a larger volume is re-simulated at significantly higher resolution, providing a substantial increase in resolution at a manageable computational cost. Such simulations can simultaneously capture the crucial baryon cycle on larger scales, while still achieving sufficiently high enough resolution to robustly model the internal structure and dynamics of galaxies.

While inflows are generally well-predicted within the ΛCDM paradigm (albeit difficult to detect), galactic outflows remain a highly uncertain and poorly constrained ingredient in galaxy formation models. It is now evident that powerful galactic outflows are ubiquitous in high-redshift galaxies, as indicated by the high frequency of blue-shifted rest-frame UV absorption lines (e.g., Weiner et al. 2009; Steidel et al. 2010; Kornei et al. 2012; Martin et al. 2012) and broad Hα emission-line profiles (e.g., Genzel et al. 2011; Newman et al. 2012). These winds carry out masses comparable to the star formation rates (SFRs; Steidel et al. 2010; Genzel et al. 2011), though these estimates can be uncertain by an order of magnitude. Hence outflows are likely to play a central role in the evolution of galaxies and the IGM.

Theoretically, outflows are the primary candidate for regulating the baryon and metal content of galaxies, while concurrently explaining the enrichment of the IGM. The physical origin and launching mechanism of such outflows is still in debate, and it is usually attributed to energy and/or momentum input from supernovae (SNe) and/or radiation pressure from massive stars (Murray et al. 2005, 2010; Krumholz & Thompson 2013). Galaxy scale and cosmological simulations by Springel & Hernquist (2003a, 2003b) showed that the injection of energy from SNe in the form of kinetic outflows with constant velocity can be effective in removing gas from galaxies, potentially solving the overcooling problem by regulating SFRs and enriching the IGM.

However, observations of dwarf starbursts and low-redshift luminous infrared galaxies (Martin 2005; Rupke et al. 2005) as well as higher redshift galaxies (Weiner et al. 2009) suggest that the properties of galactic outflows scale with galaxy properties—galaxies with higher masses and SFRs drive faster and more energetic winds—in broad agreement with predictions of momentum-driven models (Murray et al. 2005). In the momentum-driven wind scenario, radiation from massive stars is absorbed by dust that collisionally couples to the gas, resulting in galactic outflows for which the velocity and mass loading factor (i.e., the mass loss rate relative to the SFR) scale linearly and inversely, respectively, with the circular velocity of galaxies. These scalings are also favored by recent high-resolution galaxy-scale simulations including explicit stellar feedback models (Hopkins et al. 2012), though there are concerns regarding the efficiency of radiative momentum coupling required to drive sufficiently strong outflows (Dekel & Krumholz 2013; Krumholz & Thompson 2013).

Oppenheimer & Davé (2006, 2008) implemented a variety of outflow models into cosmological hydrodynamic simulations of galaxy formation, and found that the scalings arising for momentum-driven winds yielded a significant improvement over the original Springel & Hernquist (2003b) "constant wind" models toward matching a wide range of observables, including (1) the chemical enrichment of the IGM at $z > 2$ (Oppenheimer & Davé 2006, 2008), (2) the luminosity function of high-redshift galaxies (Davé et al. 2006; Finlator et al. 2007; Davé et al. 2011b), and (3) the galaxy mass–metallicity relation (Finlator & Davé 2008; Davé et al. 2011a). However, with spatial resolution of typically several kpc, these simulations were unable to examine the internal structural properties of galaxies on sub-kpc scales.

In this work, we use cosmological hydrodynamic zoom simulations including galactic outflows using the exact same prescriptions as in Davé et al. (2011b) to make predictions for internal structure and dynamics of eight re-simulated galaxies (Anglés-Alcázar et al. 2013). Our modeling is similar to that used in Genel et al. (2012b), who focused on studying the properties of star-forming clumps (Genzel et al. 2011; Förster Schreiber et al. 2011) in models with and without winds, finding that a similar wind prescription provided both realistic suppression of star formation while disrupting clumps on short timescales. Here, we examine the impact of galactic outflows on the morphological, dynamical, and star formation properties in a sample of eight re-simulated central galaxies in two re-simulated regions, and compare these properties to observations from various surveys, focusing particularly on the Spectroscopic Imaging survey in the Near-infrared with SINFONI (SINS) Survey of $z \sim 2$ galaxies (Förster Schreiber et al. 2009).

We begin by describing our simulations in Section 2 and present and overview of the sample of simulated galaxies in Section 3. We analyze the impact of galactic outflows on the time evolution and radial structure of three example galaxies in Section 4, where we also evaluate the effects of different wind models on global properties of galaxies such as halo baryonic fractions and cosmic star formation efficiencies, and their rotation curves. In Section 5 we compare the properties of our simulated galaxies to available spatially and spectrally resolved observations of $z \sim 2$ galaxies. We present resolution convergence tests of our key results in Section 6 and we summarize our results in Section 7.

2. SIMULATIONS

2.1. Simulation Code

Our simulations were run with an extended version of the *N*-body + smoothed particle hydrodynamics (SPH) cosmological galaxy formation code Gadget-2 (Springel 2005). Gadget-2 combines an entropy-conserving formulation of SPH (Springel & Hernquist 2002) along with a tree-particle-mesh algorithm for computing gravitational forces. Additions to the public version of the code have been described in Oppenheimer & Davé (2008) and include models for gas cooling, star formation, chemical enrichment, and galactic outflows.

We include photoionization heating starting at $z = 9$ via a spatially uniform, optically thin UV background (Haardt & Madau 2001). We account for radiative cooling from primordial gas assuming ionization equilibrium as in Katz et al. (1996) and metal-line cooling using the collisional ionization equilibrium tables of Sutherland & Dopita (1993). We track the production of four metal species (C, O, Si, and Fe) from Type II SNe, Type Ia SNe, and asymptotic giant branch (AGB) stars using metallicity-dependent yields as described in Oppenheimer & Davé (2008). We also account for energy feedback from Type II and Type Ia SNe, and mass loss from AGB stars.

Star formation is modeled using the sub-grid prescription of Springel & Hernquist (2003a). Gas particles that are sufficiently dense to become Jeans unstable ($n > 0.13$ cm^{-3}) are treated as a two-phase interstellar medium (ISM) consisting of hot gas that condenses into cold star-forming clouds via a thermal instability (McKee & Ostriker 1977). Stars form from the cold phase and thermal feedback from Type II SNe causes the evaporation of cold clumps into the hot medium. Star formation is implemented probabilistically, such that at any given step, a sufficiently dense gas particle can spawn a star based on a Schmidt (1959) law. The star particle's mass is half the original gas particle mass. The resulting SFRs are tuned to be in accord with the observed Kennicutt (1998a) relation.

Our simulations include a galactic outflow mechanism that imparts kinetic energy to gas particles which is identical to that used in larger-scale simulations of, e.g., Davé et al. (2011b). The outflow is described by two parameters, the wind speed v_w and the mass loading factor η, which is the mass outflow rate in units of the SFR. If a particle is eligible to form stars, it is likewise eligible to be kicked into an outflow, with a probability given by η times the star formation probability. If selected, the gas particle is kicked with a velocity v_w in the direction $v \times a$, where v and a are the particle's instantaneous velocity and acceleration. Hydrodynamic forces are turned off until the particle reaches a density of 0.013 cm^{-3}, or a time of 20 kpc$/v_w$ has passed (Oppenheimer & Davé 2008). Decoupling from hydrodynamics allows outflowing gas to escape from the galactic ISM and travel to large distances as observed in $z \approx 2$ galaxies (Steidel et al. 2010), a process not properly captured at the resolution of our simulations, and also yields results that are less sensitive to numerical resolution (Springel & Hernquist 2003b). Similar implementations of galactic outflows have been used in recent zoom simulations (Genel et al. 2012b) as well as full cosmological simulations (Barai et al. 2013; Puchwein & Springel 2013).

Choices for v_w and η define our "wind model." Throughout this paper we compare the following wind models:

1. *No wind model (nw)*: We turn-off galactic winds ($\eta = 0$).
2. *Constant wind model (cw)*: $v_{\rm w} = 680$ km s^{-1} and $\eta = 2$ for all galaxies.
3. *Momentum-driven wind model (vzw)*: The kick velocity scales with galactic velocity dispersion, σ, and the mass loading factor scales as $1/\sigma$, as in the momentum-conserving case (Murray et al. 2005). Following Oppenheimer & Davé (2008) we take $v_{\rm w} = 3\sigma\sqrt{f_{\rm L} - 1}$ and $\eta = \sigma_0/\sigma$, where $f_{\rm L}$ is the (metallicity dependent) critical luminosity necessary to expel gas from the galaxy and $\sigma_0 = 150$ km s^{-1}. We run an on-the-fly galaxy finder to calculate galaxy masses that are then converted to σ using standard relations (Mo et al. 1998).

Throughout this paper we assume a Chabrier (2003) initial mass function (IMF) and a ΛCDM concordance cosmology with parameters $\Omega_\Lambda = 0.72$, $\Omega_{\rm M} = 0.28$, $\Omega_{\rm b} = 0.046$, $h = 0.7$, $\sigma_8 = 0.82$, and $n = 0.96$, consistent with five-year *Wilkinson Microwave Anisotropy Probe* (*WMAP*) data combined with baryon acoustic oscillations and SNe constraints (Komatsu et al. 2009) as well as the final nine-year *WMAP* data (Hinshaw et al. 2013).

2.2. Simulation Runs and Analysis

Current high-resolution near-infrared observations being carried out by adaptive optics-assisted 10 m class telescopes as well as the *Hubble Space Telescope* are able to resolve ∼1 kpc scales at $z \sim 2$ (e.g., Förster Schreiber et al. 2011; Kartaltepe et al. 2012). In order to get full advantage of these observations, we used the "zoom-in" technique (e.g., Navarro & White 1994) to carry out cosmological simulations that follow the evolution of galaxies down to $z \sim 2$ with sub-kiloparsec spatial resolution. The simulations presented here have been used in Anglés-Alcázar et al. (2013) in a different context, where we constrain the growth of massive black holes at the centers of galaxies on cosmological timescales and discuss the implications of the observed black hole–galaxy correlations.

We selected two $\sim[5\,h^{-1}\,{\rm Mpc}]^3$ regions for re-simulation from an intermediate-resolution full cosmological simulation surrounding two central galaxies characterized by similar stellar masses ($\sim 3 \times 10^{10}\ M_\odot$) but different morphologies and merger histories. The parent simulation had 2×256^3 gas+dark matter particles in a $[24\,h^{-1}\,{\rm Mpc}]^3$ box and was run including momentum-driven winds. As described in Anglés-Alcázar et al. (2013), zoom initial conditions were generated by identifying all dark matter particles within the virial radius of each selected $z = 2$ galaxy, tracing their positions back to their locations on the initial grid. Refinement regions were initially defined by the grid cells containing these particles and, subsequently, significantly enlarged by an iterative cleaning procedure incorporating an increasing number of neighboring cells. High-resolution regions were populated with a large number of lower mass particles (yielding ×64 mass resolution increase for our highest resolution simulations) and small-scale power spectrum fluctuations were applied according to the spatial resolution of the refined grid. Additionally, two nested concentric layers of progressively lower resolution were defined surrounding the high-resolution regions in order to reduce numerical artifacts due to the difference in particle masses and to ensure that the large-scale gravitational torques acting on re-simulated halos are accurately represented.

The resulting zoom simulations have (high-resolution) gas particle mass $m_{\rm gas} \approx 2.3 \times 10^5\ M_\odot$, dark matter particle mass $m_{\rm DM} \approx 1.2 \times 10^6\ M_\odot$, and softening length $\epsilon \approx 0.47\,h^{-1}$ kpc comoving (∼224 pc physical at $z = 2$), equivalent to 2×1024^3 particles homogeneously distributed in a $[24\,h^{-1}\,{\rm Mpc}]^3$ box. Additionally, we run similar zoom simulations with a factor of 2 lower spatial resolution and a factor of eight lower mass resolution in order to test our results for numerical convergence. A total of 215 snapshot files logarithmically spaced in the redshift range $z = 2$–11 were produced for each simulation, corresponding to time intervals ranging from ∼5 to 25 Myr.

Galaxies were identified by means of the Spline Kernel Interpolative Denmax algorithm (SKID[8]) at all available snapshots independently, and are thus defined as bound groups of star-forming gas particles (i.e., gas particles with densities above the threshold for star formation) and star particles (see Kereš et al. 2005). We used a spherical overdensity algorithm to associate each SKID-identified galaxy with a dark matter halo, where the virial radius was defined to enclose a mean density given by Kitayama & Suto (1996). Overlapping halos were grouped together so that every final halo has a central galaxy and a number of satellite galaxies by construction.

The sample of galaxies presented here was defined by selecting the eight most massive central galaxies located within the re-simulated volumes, with the additional requirement of having no contamination by low-resolution dark matter particles

[8] http://www-hpcc.astro.washington.edu/tools/skid.html

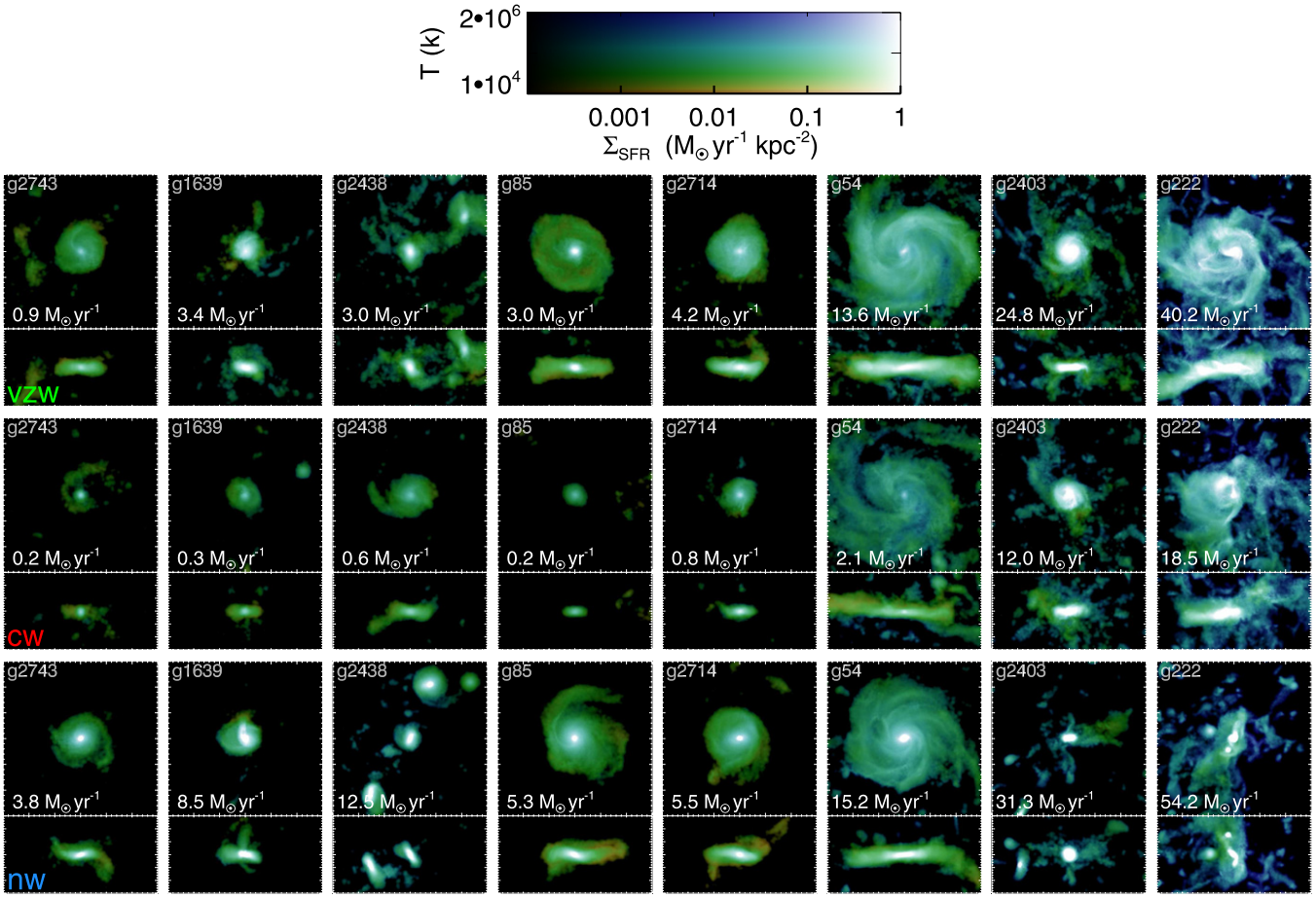

Figure 1. Star formation rate surface density maps color-coded according to the projected density-weighted temperature for our eight re-simulated galaxies at $z = 2$. For each galaxy, we show the projected gas distributions corresponding to simulations including momentum-driven winds (top), constant winds (middle), and no winds (bottom). Face-on and edge-on views of each galaxy correspond to the total angular momentum of the gas component. Galaxies are ordered from left to right for increasing stellar mass according to simulations with momentum-driven winds (with total halo masses ranging from $\sim 10^{11}$ to 2×10^{12} $M_\odot$). Total SFRs are listed for all galaxies and wind models. The region shown is 30 kpc (physical) across.

(A color version of this figure is available in the online journal.)

within their virial radius; several central galaxies were located near the boundaries of the high-resolution region and were rejected because of contamination. Even though this sample is not mass nor volume complete, our galaxies are representative of "normal" $z = 2$ systems, with similar gas fractions and SFRs relative to similar mass galaxies from the parent population.

The full evolution of each $z = 2$ galaxy was reconstructed by identifying its most massive progenitor at all available redshift snapshots. Galaxies were also identified across simulations with different wind models to allow for a detailed model comparison. Following Anglés-Alcázar et al. (2013), we calculated structural and kinematic properties of each galaxy relative to the position of its most bound gas particle, which is a more meaningful and more stable definition of the nominal center of the galaxy compared to that computed by SKID, especially during close galaxy encounters and galaxy mergers.

3. GALAXY SAMPLE

We begin by describing the sample of eight galaxies used in this work. At $z = 2$, the masses of dark matter halos range from $\sim 10^{11}$ to 2×10^{12} $M_\odot$ and are typically resolved with $\sim 2 \times 10^5$ to 4×10^6 particles. As we describe in detail throughout this paper, galaxy properties are highly dependent on the model adopted for galactic outflows. For our fiducial simulations including momentum-driven winds (vzw model), galaxies have stellar masses ranging from $\sim 1.6 \times 10^9$ to 3.3×10^{10} $M_\odot$ and SFRs in the range $\sim$1–40 $M_\odot$ yr^{-1} at $z = 2$. Figure 1 shows face-on and edge-on views of the star-forming gas of galaxies at $z = 2$. Our galaxy sample spans a wide range of sizes and morphologies, with the star-forming gas extending up to scales of 2–15 kpc from their centers. Some galaxies are located in high density environments and undergo frequent interactions and mergers (e.g., galaxy g222) while others are characterized by a smoother evolution, in lower density environments (e.g., galaxy g54). Despite this, most galaxies appear to be rotationally supported disks at $z = 2$. Figure 2 shows the projected stellar distribution corresponding to the same galaxies. Stellar disks can also be visually identified for most galaxies but in this case a higher fraction of stars seems to correspond to a spheroidal component.

Galaxies are identified across the various wind simulations via their halos, making it possible to analyze the effects of galactic winds in a galaxy-by-galaxy basis. However, when comparing the morphologies of galaxies across wind models it is important to note that galaxy interactions and mergers are inherently random processes. Small deviations of orbital parameters in different simulations can result in rather different morphologies at a given time, and therefore it is not trivial to compare morphological features such as spiral arms or

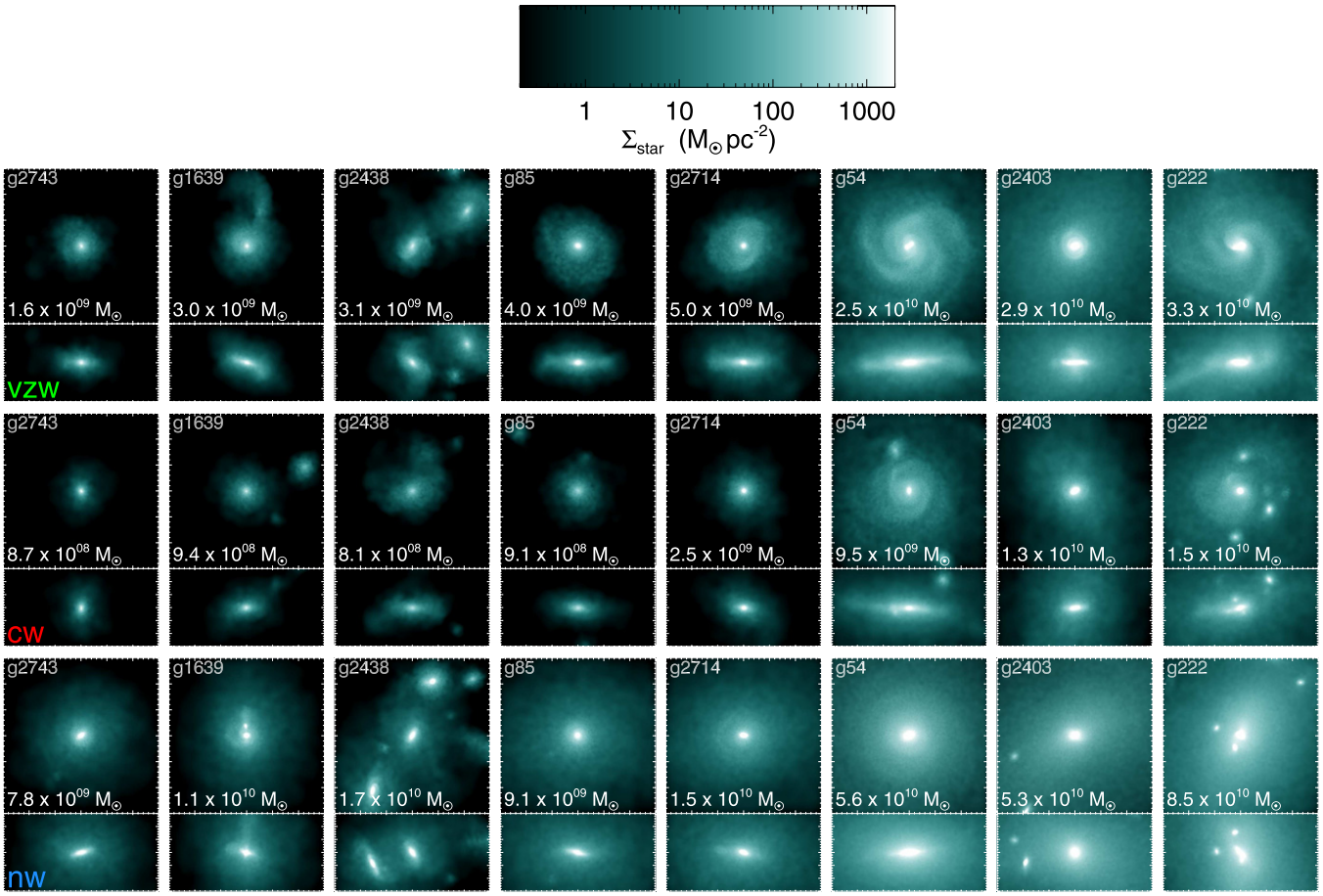

Figure 2. Same as Figure 1 for the projected stellar surface density. Total stellar masses are listed for all galaxies and wind models.
(A color version of this figure is available in the online journal.)

tidal tails among the different models (e.g., galaxies g1639, g2438, g85, and g54). Despite this, a quick visual inspection of Figures 1 and 2 reveals significant differences between wind prescriptions. Constant winds are very efficient in removing gas from galaxies and result in lower mass galaxies with typically lower SFR surface densities compared to the momentum-driven winds. This is particularly evident in the low mass range, where the formation of large-scale disks of star-forming gas is highly suppressed (e.g., galaxies g2743 and g85). In contrast, simulations with no winds usually form more massive and more concentrated galaxies compared to the vzw model, with most of the star formation happening in the central regions of galaxies.

4. THE EFFECTS OF WINDS

4.1. Time Evolution

Each galaxy is identified not only across simulations with different wind models but also back in time at all available snapshots, as the central galaxy in the resimulated halo. Figure 3 shows examples of the time evolution of galaxies in terms of their stellar mass, gas fraction, SFR, and metallicity. Since we are interested in the evolution of galaxies over cosmological timescales, the time evolution of all physical quantities has been smoothed over time intervals of ∼50 Myr. Major mergers can still be identified as abrupt changes in the stellar mass of galaxies (e.g., galaxy g222 between redshifts $z = 2$–3 and g54 at $z \approx 4$). These events are generally followed by a temporary increase in the SFR of galaxies but their overall evolution is dominated by smooth accretion, as has been reported for simulations of high-redshift galaxies elsewhere (e.g., Dekel et al. 2009; Davé et al. 2010).

Simulations with no winds clearly result in higher stellar masses for all galaxies at all times. Very early on, the SFR of galaxies increases very rapidly for simulations with no winds. When galactic outflows are included, galaxies regulate themselves resulting in significantly lower SFRs relative to the no wind model at $z > 3$. For momentum-driven winds, recycling of the outflowing gas back into galaxies occurs on a timescale less than the Hubble time, providing an additional gas supply which is not available in simulations with no winds (Oppenheimer & Davé 2010). This additional gas supply results in comparatively higher SFRs toward the end of the simulation at $z = 2$. Constant winds are, however, more efficient in removing cold gas from galaxies owing to the higher outflow velocities ($v_w = 680$ km s^{-1}) for comparatively similar mass loading factors ($\eta = 2$)—for the three most massive systems in our galaxy sample (g222, g2403, and g54), we find typical wind velocities $v_w \approx 500$–600 km s^{-1} and mass loadings $\eta \approx 1.4$–1.9 in the redshift range $z = 8 \rightarrow 2$ for the momentum conserving model. This results in systematically lower SFRs for the constant wind model at all times.

Interestingly, specific SFRs follow a common trend regardless of the wind model adopted: galaxies have the highest specific SFRs very early on (as high as 10 Gyr^{-1} at $z = 8$) and then decrease monotonically with decreasing redshift. To first order, outflows reduce SFRs by a factor $1/(1 + \eta)$ relative to halo accretion rates (Davé et al. 2012), which leads to specific SFRs that remain the same across wind models (SFRs and stellar

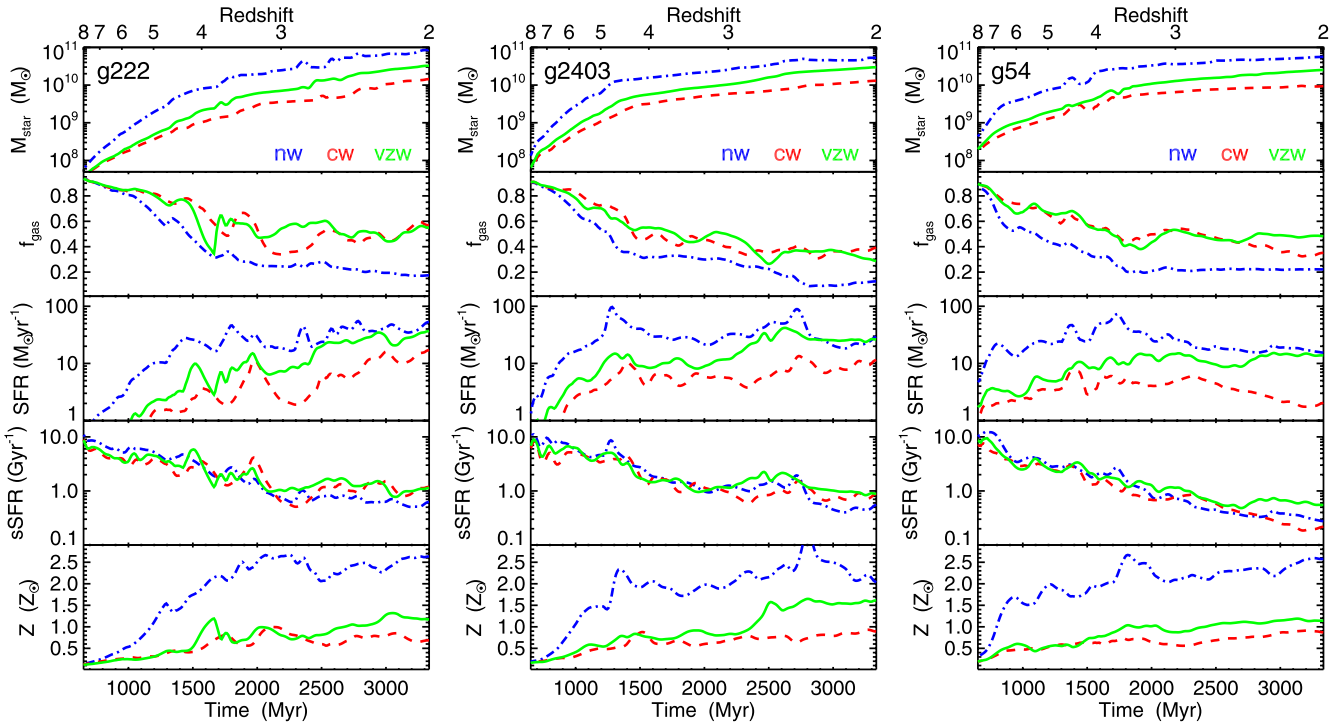

Figure 3. Time evolution of galaxies g222, g2403, and g54 from $z = 8$ to $z = 2$ for simulations including models for momentum-driven winds (green solid lines), constant winds (red dashed lines), and no winds (blue dot-dashed lines). From top to bottom: stellar mass, gas fraction, star formation rate, specific star formation rate, and average gas phase metallicity (SFR-weighted). The time evolution of all physical quantities has been smoothed over time intervals of ∼50 Myr.

(A color version of this figure is available in the online journal.)

masses are reduced by the same amount). Wind recycling accretion, however, yields increasing specific SFRs at later times, especially in the momentum-driven wind model.

Gas fractions are systematically lower for the no wind simulations compared to either the constant wind or the momentum-driven wind models. While galaxies g222, g2403, and g54 have gas fractions below 20% for simulations with no winds at $z = 2$, galactic outflows are able to maintain gas fractions a factor of two higher at the end of the simulation, in better agreement with observations (Tacconi et al. 2010). Gas fractions may be conveniently expressed in terms of the depletion time $t_{dep} \equiv M_{gas}/SFR$ and the specific SFR as $f_{gas} \equiv [(1+(t_{dep}sSFR)^{-1})]^{-1}$ (Davé et al. 2012). Since specific SFRs are roughly insensitive to wind model early on and the depletion time is shorter in higher stellar mass galaxies ($t_{dep} \propto M_*^{-0.3}$; Davé et al. 2011a), no wind simulations yield lower gas fractions.

Finally, metallicities are significantly higher for all galaxies in the no wind model, owing to a greater conversion of baryons into stars and a lack of ejection of metals into the IGM (Hirschmann et al. 2013). These results are qualitatively consistent with those obtained using lower-resolution non-zoom cosmological runs (Davé et al. 2011b, 2011a).

4.2. Radial Profiles

The radial profiles of galaxies reveal interesting differences among wind models, as shown in Figure 4 for galaxies g222, g2403, and g54 at $z = 2$. Face-on projected stellar and gas surface densities, circular velocity, and metallicity as a function of radial distance from the centers of galaxies have been calculated as average values within logarithmically spaced radial bins. The most massive galaxies (g222 and g2403) reach resolved stellar and gas surface densities in the range $\Sigma_{star} = 10^4$–10^5 $M_\odot$ pc^2 and $\Sigma_{gas} = 10^3$–10^4 $M_\odot$ pc^2 respectively, with differences up to an order of magnitude among wind models. At their centers, stellar surface densities of most galaxies reach values well above 10^3 $M_\odot$ pc^2 despite gravitational forces being softened at scales $\sim\epsilon \approx 224$ pc (Figure 2).

No wind simulations usually result in higher stellar surface densities at all radii compared to the vzw and cw wind models, and often steeper density gradients at the centers of galaxies. The effects of galactic winds are, however, more evident in the distribution of the star-forming gas: nw galaxies contain most of their gas within the inner kiloparsec, reaching gas surface densities which can be factors of a few above the cw and vzw models. Galactic winds yield more extended disks by removing gas from their centers and having it re-accreted at larger scales. Wind recycling, especially in the vzw model, results in significant amounts of gas extending up to a few kiloparsecs away from the galaxy center (see galaxies g222 and g54 in Figure 4). As we show in the next sections, this result is common to most of our simulated galaxies. Galaxy g2403 is one of the few galaxies that present a very compact gas distribution even in the presence of momentum-driven winds, similar to galaxies from simulations with no galactic outflows.

Most of our simulated galaxies are characterized by flat rotation curves extending up to a few kiloparsecs. The no wind model usually produces more massive and more compact galaxies and this results in higher circular velocities that peak at smaller radii compared to the vzw and cw models. Simulations with winds produce more smoothly rising rotation curves, with lower circular velocities at small radii that tend to approach values similar to the nw model at larger scales, where the contribution from the dark matter component becomes dominant (see galaxies g222 and g54 in Figure 4; this is explored in more detail in Section 4.4). Galaxy g2403 is again an atypical case, with very similar rotation curves for the nw and vzw wind models.

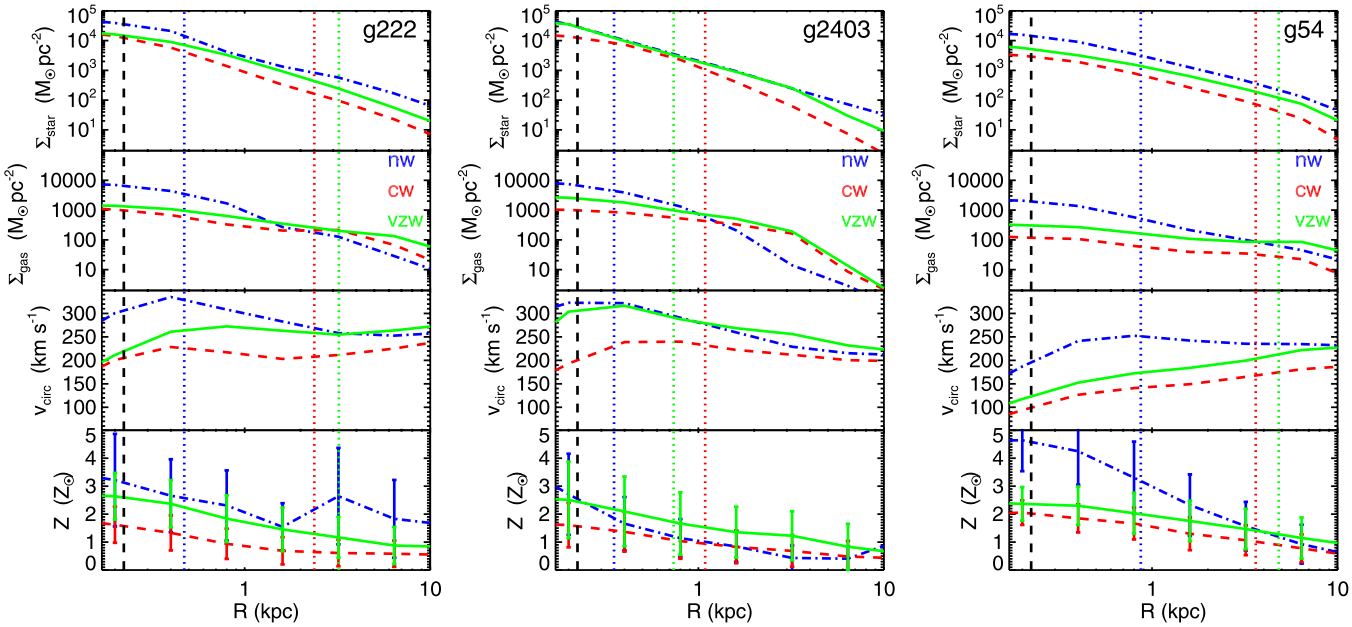

Figure 4. Radial profiles of galaxies g222, g2403, and g54 at $z = 2$ for simulations including models for momentum-driven winds (green solid lines), constant winds (red dashed lines), and no winds (blue dot-dashed lines). From top to bottom: azimuthally averaged face-on stellar and gas surface densities, circular velocity (calculated as $v_{\rm circ}^2 = GM_{\rm enc}(r)/r$ for the enclosed mass $M_{\rm enc}(r)$ within radius r), and average gas phase metallicity (SFR-weighted). Error bars in the bottom panel indicate the spread of the particle distribution within each radial bin for each galaxy. Black vertical dashed lines show the softening length of the simulation at $z = 2$ ($\epsilon \approx 224$ pc physical) while the green, red, and blue vertical doted lines correspond to the radius enclosing half of the total SFR for the different wind prescriptions.

(A color version of this figure is available in the online journal.)

Finally, negative radial gas-phase metallicity gradients (higher metallicities at the centers of galaxies) are common in most simulated galaxies, in general agreement with observations (Yuan et al. 2011; Swinbank et al. 2012b; Jones et al. 2013). Nonetheless, inverted metallicity gradients have been observed in $z \sim$ 2–3 galaxies and attributed to either galaxy interactions or the infall of metal-poor gas into the centers of galaxies (Cresci et al. 2010; Queyrel et al. 2012; Troncoso et al. 2013). In our simulations, abrupt changes in azimuthally averaged metallicities or even positive metallicity gradients may eventually occur for galaxies undergoing mergers (e.g., galaxy g222 at $R \approx$ 3–4 kpc). Overall, we find that simulations with no winds usually result in higher metallicities at all radii and also show steeper metallicity gradients. Galactic outflows serve to redistribute metal-enriched gas from the central regions of galaxies over larger scales, resulting in less steep metallicity gradients.

4.3. Connecting Individual Halos Across Wind Models

In order to understand the global effects of galactic winds it is useful to look at their effects on different galaxy properties at fixed halo mass, since the latter is expected to be roughly insensitive to baryonic processes. In Figure 5, we plot the halo baryonic fraction, the central stellar mass to halo mass fraction, and the SFR as a function of halo mass for all simulated galaxies at $z = 2$. Here, each vzw galaxy is connected to the corresponding nw and cw galaxies to help identify both the global effects of outflows on the galaxy population as well as the effects on individual galaxies. Total halo masses are very similar for the nw and vzw models at $z = 2$, except occasionally due to the slightly different timing of merger events and our adopted definition of dark matter halos for each central galaxy (see Section 2). Halo masses are, however, systematically lower for simulations with constant winds, for which gas outflows are able to escape more easily from the halo potential well, all of which generally have escape velocities below the constant wind velocity of $v_w = 680$ km s^{-1}. Note that momentum-driven wind velocities are below that of the cw model in all but the most massive galaxies, especially at high redshift when galactic velocity dispersions are lower (Oppenheimer & Davé 2008).

Figure 5 shows that halo baryonic fractions are only slightly higher for the no wind model (and higher on average than the cosmological baryonic fraction $f_b = 0.165$) compared to the vzw model: most of the outflowing gas does not escape the halo potential well for the momentum-driven wind model. This is despite the fact that the wind speed typically is comparable to or exceeding the escape velocity (and scales with it as well); but hydrodynamic (i.e., ram pressure) slowing is actually dominant in many cases (Oppenheimer & Davé 2008). In contrast, the high efficiency of constant winds in expelling gas from halos results in systematically lower halo baryonic fractions, a significant suppression of star formation in the central galaxy, and the consequent reduction of stellar masses for all galaxies in our sample.

Figure 5 (middle panel) confirms our earlier expectations: for a given halo mass, central galaxy stellar masses are systematically higher in the absence of galactic outflows. Interestingly, SFRs for the nw and vzw models happen to be similar at $z = 2$ for most simulated galaxies. However, as we have seen in Figure 3 for galaxies g222, g2403, and g54, momentum-driven winds result in rather different star formation histories, with significant suppression of star formation early on and enhanced activity due to wind recycling at later times (Oppenheimer & Davé 2010). The wind recycling channel does not act on the cw simulations for the range of halo masses probed here, since these halos generally have escape velocities lower than the assumed wind speed.

Figure 6 illustrates the effects of galactic winds in the star formation histories of our simulated galaxies by showing the evolution of the cosmic star formation efficiency (cSFE) in the redshift range $z =$ 2–6. The cSFE is the ratio of the SFR

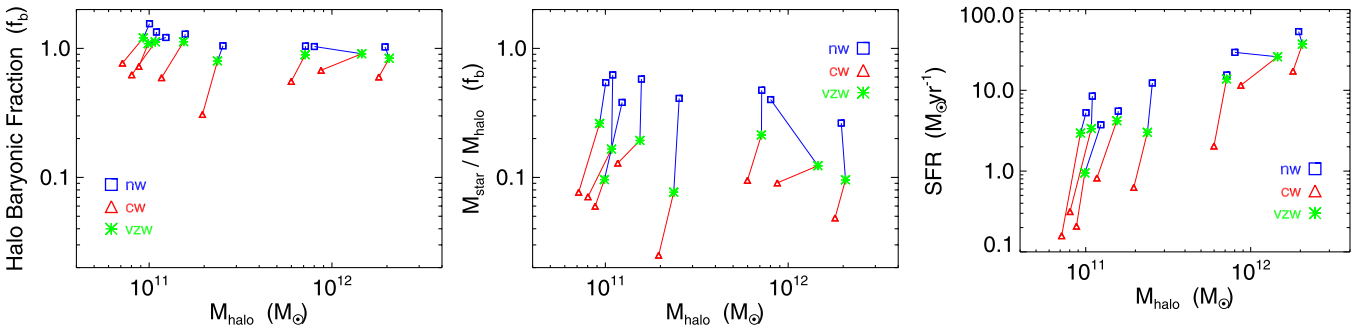

Figure 5. Effects of galactic winds on global properties of $z = 2$ galaxies and their parent halos as a function of halo mass. Left: total halo baryonic fraction in units of the cosmological baryonic fraction ($f_b = 0.165$). Middle: ratio of central stellar mass to halo mass in units of f_b. Right: central galaxy star formation rate. Galaxies from simulations including momentum-driven winds (vzw), constant winds (cw), and no winds (nw) are shown as green star symbols, red triangles, and blue squares respectively. Red and blue solid lines connect galaxies from the vzw simulations with their galaxy counterparts from the cw and nw simulations respectively.

(A color version of this figure is available in the online journal.)

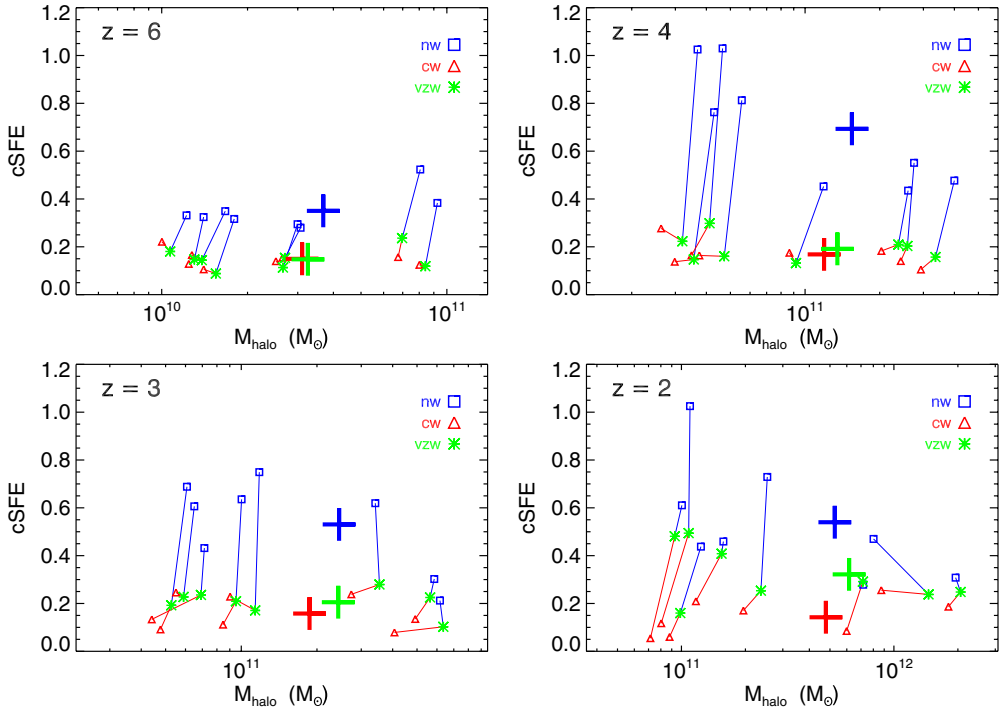

Figure 6. Evolution of the cosmic star formation efficiency, i.e., the ratio of the central galaxy SFR to the total halo baryonic accretion rate (Dekel et al. 2009) from $z = 6$ to $z = 2$ as a function of halo mass for all simulated galaxies and for the different wind prescriptions. Lines and colors are as in Figure 5. Green, red, and blue crosses show the average cSFE and halo mass for the momentum-driven winds, constant winds, and no wind models respectively.

(A color version of this figure is available in the online journal.)

of the central galaxy to the total halo baryonic accretion rate given in Dekel et al. (2009):

$$\dot{M}_{\rm acc} \simeq 6.6\, f_{\rm b}\, (M_{\rm halo}/10^{12} M_{\odot})^{1.15}\, (1+z)^{2.25}\, M_{\odot}\, {\rm yr}^{-1}. \quad (1)$$

At $z = 6$, the average cSFE of galaxies for simulations including outflows (cw and vzw models) is ~0.15, about a factor of two lower than simulations with no winds. From $z = 6$ to $z = 4$, the average cSFE increases rapidly up to ~0.69 for nw simulations, and then decreases down to ~0.54 at $z = 2$. Simulations with constant winds seem to follow a similar tendency, with the average cSFE peaking at $z \sim 4$–5 and decreasing at lower redshifts, but with significantly lower values (roughly $\times 3$, as expected from the $(1+\eta)$ suppression of star formation). Momentum-driven winds result, however, in an overall increase of cSFEs from $z = 6$ to $z = 2$, owing to the recycling of gas that was launched into winds at earlier times. The vzw model causes an effective delay in star formation by ejecting significant amounts of gas from small, early galaxies and having it reaccreted by $z \sim 2$. This coincidentally produces average SFRs similar to simulations with no winds at $z \approx 2$. Note that trends for individual galaxies mimic the trends for the overall cosmic star formation history in these wind models, with momentum-driven winds generally producing a later peak in cosmic SFR than no-wind or constant-wind cases (Oppenheimer & Davé 2006).

4.4. Rotation Curves

Galaxy rotation curves contain substantial information about the structure and kinematics of galaxies. Figure 7 (top panel) shows the rotation curves of all simulated galaxies at $z = 2$ (dotted lines), color-coded by wind model. Here, we calculate the rotation velocity from the enclosed mass at a given radius,

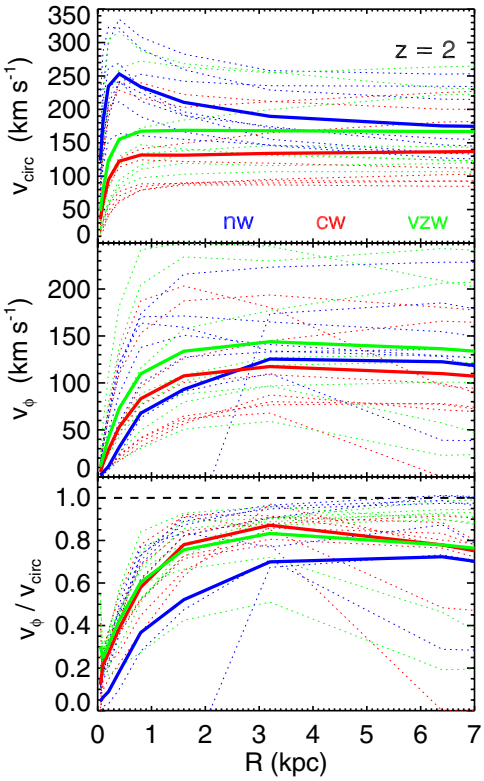

Figure 7. Top: circular velocity ($v_{\rm circ}$) as a function of radial distance from the center of simulated galaxies at $z = 2$. We compute $v_{\rm circ}^2 = GM_{\rm enc}(r)/r$ for the total enclosed mass $M_{\rm enc}(r)$ within distance r. Middle: azimuthal velocity (v_ϕ) of the gas particles with respect to the total angular momentum of the galaxy averaged within logarithmically spaced radial bins (SFR-weighted). Bottom: ratio of the average azimuthal velocity of the gas to the circular velocity as a function of radial distance from the center of galaxies. Green, red, and blue dotted lines show rotation curves of individual galaxies (or the ratio $v_\phi/v_{\rm circ}$) for the momentum-driven winds, constant winds, and no wind models respectively. Thick solid lines show the rotation curve (or $v_\phi/v_{\rm circ}$) averaged over all galaxies corresponding to each wind model.

(A color version of this figure is available in the online journal.)

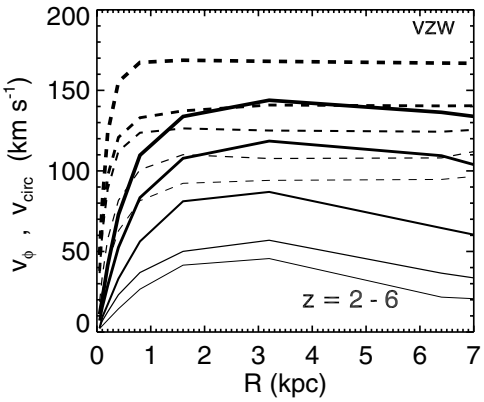

Figure 8. Build up of the galaxy rotation curves as a function of redshift from $z = 6$ (thin grey line) to $z = 2$ (thick black line) for simulations including momentum-driven winds. Dashed lines show the circular velocity ($v_{\rm circ}$) averaged over all galaxies (as in Figure 7, top panel) while solid lines show the actual gas azimuthal velocity (v_ϕ) averaged within each radial bin (and again averaged over all vzw galaxies).

which we call $v_{\rm circ}$. Our galaxies are characterized by flat rotation curves extending up to several kpc scales, with asymptotic circular velocities ranging from ∼100 to 260 km s^{-1} at $z = 2$ for the vzw model. In Figure 4, we showed for galaxies g222, g2403, and g54 that galactic outflows can have a significant impact on the overall shape of their rotation curves.

The thick solid lines in Figure 7 (top panel) show stacked rotation curves for each wind model, where circular velocities have been averaged over all galaxies as a function of radius. Simulations with winds produce galaxies with more gradually rising rotation curves compared to the more centrally peaked rotation curves of galaxies with no winds. The average circular velocities for the nw and vzw models tend to approach similar values at larger radii, where the contribution from the dark matter component becomes dominant. Simulations with constant winds are more efficient in removing gas from halos, resulting in systematically lower asymptotic circular velocities, but their shape is similar to the momentum-driven winds.

The middle panel of Figure 7 shows a more observationally motivated way of calculating the rotation curve. Rather than taking the enclosed mass and assuming full rotational support, here we directly calculate the SFR-weighted azimuthal velocities of gas particles with respect to the total angular momentum of the galaxy, and average them within logarithmically spaced radial bins, which we call v_ϕ. This is analogous to an Hα rotation curve. The rotation curves derived in this way show a significantly more gradual increase in circular velocity with radius in the inner parts, because of the increased dispersion support in the central regions. This is particularly clear for simulations with no winds, which produce more compact galaxies and centrally peaked rotation curves based on the mass profiles.

The bottom panel of Figure 7 shows the ratio of $v_\phi/v_{\rm circ}$. We see that the gas azimuthal velocity is, on average, lower than the inferred circular velocities. The gas reaches rotation velocities comparable to the circular velocity at ∼3 kpc away from the centers of galaxies. In the inner regions, the contribution of random motions to the dynamical equilibrium of galaxies becomes comparable to the support from ordered rotation. The discrepancy between v_ϕ and $v_{\rm circ}$ at scales <3 kpc occurs for all simulated galaxies and wind models, and it is well resolved in our simulations. Using v_ϕ to infer the mass profile of galaxies could, therefore, lead to significant misestimations (Valenzuela et al. 2007).

Figure 8 shows the build-up of rotation curves with time by comparing stacked rotation curves from $z = 6$ to $z = 2$ for our simulations with momentum-driven winds. Solid lines show v_ϕ (for the gas), and dashed lines show $v_{\rm circ}$. We find that the average asymptotic circular velocities increase from ∼90 to 170 km s^{-1} with decreasing redshift, as expected because our galaxies are becoming more massive. For $v_{\rm circ}$, the peak of the (average) rotation curve is always at ∼1–2 kpc, perhaps moving inward to lower redshifts. In contrast, the location of the peak of v_ϕ occurs at 3–4 kpc, and does not vary much with redshift. Comparing v_ϕ to $v_{\rm circ}$, we see that gas azimuthal velocities are, on average, lower than the inferred circular velocities at all redshifts. The ratio $v_\phi/v_{\rm circ}$ evaluated at $R \approx 3$ kpc increases from ∼0.48 at $z = 6$ to ∼0.86 at $z = 2$, indicating that galaxies become, on average, progressively more rotationally supported with time (and therefore with increasing mass) in the redshift range $z = 6 \rightarrow 2$.

5. COMPARISON TO OBSERVATIONS

The high resolution afforded by Hubble probing both young stars and older stellar populations, together with adaptive optics-enhanced spectral studies from the ground, have opened up new windows into high-redshift galaxy assembly. Here we examine

both qualitatively and quantitatively how our simulated galaxies compare with the latest observations of $z \sim 2$ galaxies.

5.1. Qualitative Galaxy Morphologies

We begin by considering in detail the morphology of the two galaxies that were specifically chosen for resimulation, g54 and g222, and therefore lie near the center of the zoomed region. Recall that g54 was chosen to be somewhat more isolated and have a fairly quiet merger history, while g222 lived in a denser region with a more violent merger history.

Figure 9 shows two-dimensional projected views of galaxy g54 at four different inclination angles. The top three rows show the stellar surface density, gas surface density, and SFR density distributions resulting from our fiducial simulation including momentum-driven winds. The three bottom rows show mock Hα line intensity, line-of-sight velocity, and velocity dispersion maps of galaxy g54 that mimic the resolution of current near-infrared integral field spectroscopic observations with SINFONI. Simulated SFRs have been converted to Hα luminosity using $L_{\mathrm{H}\alpha}[\mathrm{erg\,s^{-1}}] = 2.3 \times 10^{41}\,\mathrm{SFR}\ [M_\odot\ \mathrm{yr^{-1}}]$ (from Kennicutt 1998b, corrected for a Chabrier (2003) IMF). Then, mock Hα line intensity maps have been obtained by (1) placing the simulated galaxy at $z = 2$, converting its physical size to its apparent angular size, (2) convolving the obtained Hα flux map with a 0.″17 beam, and (3) matching the pixel size to those of typical observations (0.″05 $\mathrm{pix^{-1}}$). Mock Hα flux-weighted line-of-sight velocity and velocity dispersion maps have been obtained by degrading the spatial resolution in a similar way.

With stellar mass $\sim 2.5 \times 10^{10}\ M_\odot$, gas fraction $f_{\mathrm{gas}} \approx 0.48$, and SFR $\sim 13.6\ M_\odot\ \mathrm{yr^{-1}}$, galaxy g54 has a prominent two-arm spiral structure extending up to $\sim$10 kpc scales that could be observable even at high inclination angles ($i \leqslant 60^\circ$). Star-forming gas and stars generally trace the same structure, though the stars show a prominent bulge that is absent in the gaseous component. Mock Hα line intensity maps show a somewhat compact central nucleus with radius $\sim$1 kpc and a factor $\sim$2 increased brightness relative to the spiral arms (depending on inclination angle). Observations using star formation tracers and rest-frame optical observations should, thus, infer similar spiral morphologies. The velocity maps illustrate the effects of the inclination angle on the observed kinematic properties of galaxies. A very smooth velocity gradient along the morphological major axis can be clearly identified for this galaxy at a wide range of inclination angles ($i \geqslant 30^\circ$). Interestingly, galaxy g54 shows a characteristic "spider diagram" pattern in the velocity iso-contours at intermediate inclination angles ($i \approx 30^\circ$–60°), as expected for inclined rotating disks. For nearly edge-on observations, line-of-sight projected peak-to-peak velocities reach values >400 km $\mathrm{s^{-1}}$, consistent with the circular velocity $v_{\mathrm{circ}} \approx 230$ km $\mathrm{s^{-1}}$ calculated at the outer edge of the disk ($R \sim 10$ kpc). With a relatively flat velocity dispersion map, this galaxy would be identified as a large, thick, rotation-dominated disk. These properties are in general quite similar to, though somewhat scaled down from BX442, the $z = 2.18$ grand design spiral observed by Law et al. (2012). BX442 has a measured stellar mass $\sim 6 \times 10^{10}\ M_\odot$, H$\alpha$-derived SFR $\sim 45\ M_\odot\ \mathrm{yr^{-1}}$, inclination-corrected circular velocity $v_{\mathrm{circ}} \approx 234$ km $\mathrm{s^{-1}}$, and very similar size and morphology compared to our simulated galaxy g54.

Figure 10 shows similar two-dimensional maps for galaxy g222, a marginally higher mass galaxy that has undergone more frequent interactions and mergers. Indeed, there is an infalling galaxy along the lower spiral arm, which is prominent in the stellar distribution but much less evident in the gas, possibly because its gas has been stripped during infall. The stellar surface density distribution shows a high concentration of stars at the center of g222 and possibly a weak, extended spiral structure. The gas and SFR distributions reveal high levels of turbulence on this galaxy. The morphology of g222 appears highly disturbed in Hα emission and it does not seem to trace the smooth stellar component as in the case of g54. The velocity maps show signs of ordered rotation in the underlying large-scale gas distribution at high inclination angles ($i \geqslant 60^\circ$), but the inferred velocity gradients are significantly disturbed. The velocity dispersion map reveals an irregular gas clumpy structure with significant turbulent motions. The Hα shows up to several clumps, depending on the viewing angles, but these clumps are not apparent in the stellar distribution, which suggests these are short-lived gaseous clumps as found in similar simulations by Genel et al. (2012b), and as inferred in observations by Wuyts et al. (2012); we will examine clump properties in more detail in future work. Overall, this simulated galaxy shares various characteristic morphological and kinematic properties with typical clumpy disk galaxies observed at $z \sim 2$ (Förster Schreiber et al. 2009, 2011; Genzel et al. 2011; Swinbank et al. 2012a, 2012b).

Note, however, that star formation in our simulated galaxies appears to be in general more centrally concentrated than observed $z \sim 2$ disk galaxies (Figure 1), for which a central Hα peak is sometimes not present, particularly for less massive galaxies. This might be partially explained by obscuration effects, which will be quantified in future work in order to make a more detailed comparison between observed Hα line intensity maps and the intrinsic SFR surface density distribution of simulated galaxies. One numerical issue is that the pressurized ISM resulting from the star formation prescription (Springel & Hernquist 2003a) may inhibit the formation of off-center clumps by gravitational instability, especially in galaxies undergoing a more quiescent evolution. Despite this, the two example galaxies presented here—with stellar masses $M_{\mathrm{star}} > 10^{10}\ M_\odot$ that are actually comparable to commonly observed $z \sim 2$ systems—illustrate the wide diversity in morphologies predicted in these simulations, as well as its dependence on tracer (gas, stars, Hα). Disk structures are usually present, but can range from quiescent "grand-design" spirals to turbulent and clumpy disks.

5.2. Comparison to SINS and SHiZELS

We now conduct a more quantitative comparison to the structural and dynamical properties of $z \sim 2$ galaxies inferred from near-infrared integral field spectroscopic observations obtained with SINFONI at the Very Large Telescope. In particular, we focus on the "Hα sample" of the SINS survey presented in Förster Schreiber et al. (2009), consisting of 62 rest-frame UV/optically selected star-forming galaxies at $z \approx 1.5$–2.5, and the SHiZELS survey (Swinbank et al. 2012b), consisting of nine Hα-selected galaxies at $z \approx 0.84$–2.23 drawn from the HiZELS near-infrared narrow-band survey (Geach et al. 2008). In Figure 11, we show some key structural and dynamical quantities versus stellar mass, for our simulated galaxies color-coded by wind model, as well as for the SINS (black crosses) and SHiZELS (brown diamonds) samples.

The upper left panel of Figure 11 shows the specific SFR as a function of stellar mass for our sample of galaxies at $z = 2$. Our simulations naturally predict the existence of a correlation between galactic SFRs and stellar masses, $M_\star \propto \mathrm{SFR}$, fairly insensitive to stellar feedback models, due to the dominance

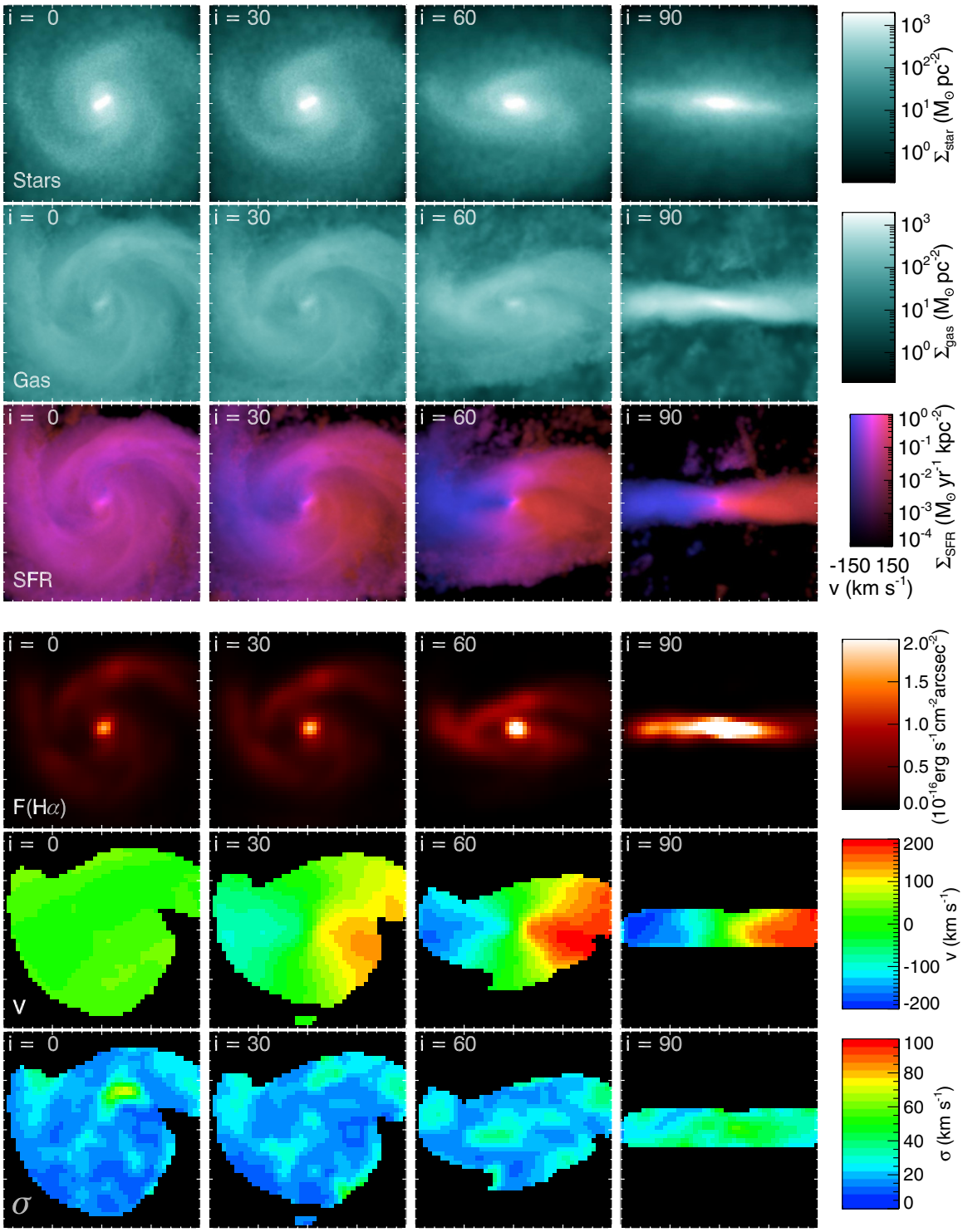

Figure 9. Morphological and kinematic properties of galaxy g54 at $z = 2$ for our fiducial simulation including momentum-driven winds. Upper panels show (from top to bottom) the projected stellar surface density, gas surface density, and SFR surface density color coded by (SFR-weighted) line-of-sight velocity. Lower panels show (from top to bottom) mock Hα line intensity, line-of-sight velocity, and one-dimensional projected velocity dispersion maps that mimic integral field unit observations with SINFONI. Two-dimensional projected images and mock maps are shown at different inclination angles, from direct face-on (left) to edge-on (right). The region shown is 20 kpc (physical) across.

(A color version of this figure is available in the online journal.)

of smooth and steady cold accretion (e.g., Finlator et al. 2006; Davé 2008; Davé et al. 2011b). As expected from models, a tight $M_\star$–SFR relation has been observed out to $z \sim 2$, with a roughly constant slope close to unity (e.g., Daddi et al. 2007; Elbaz et al. 2007; Noeske et al. 2007). However, the observed normalization of this relations increases more rapidly with redshift from $z = 0 \rightarrow 2$ that current cosmological simulations predict, resulting in too low predicted specific SFRs at $z \sim 2$ (Daddi et al. 2007; Davé 2008). Our zoom simulations follow this trend—Figure 11 shows that they lie below the $M_\star$–SFR

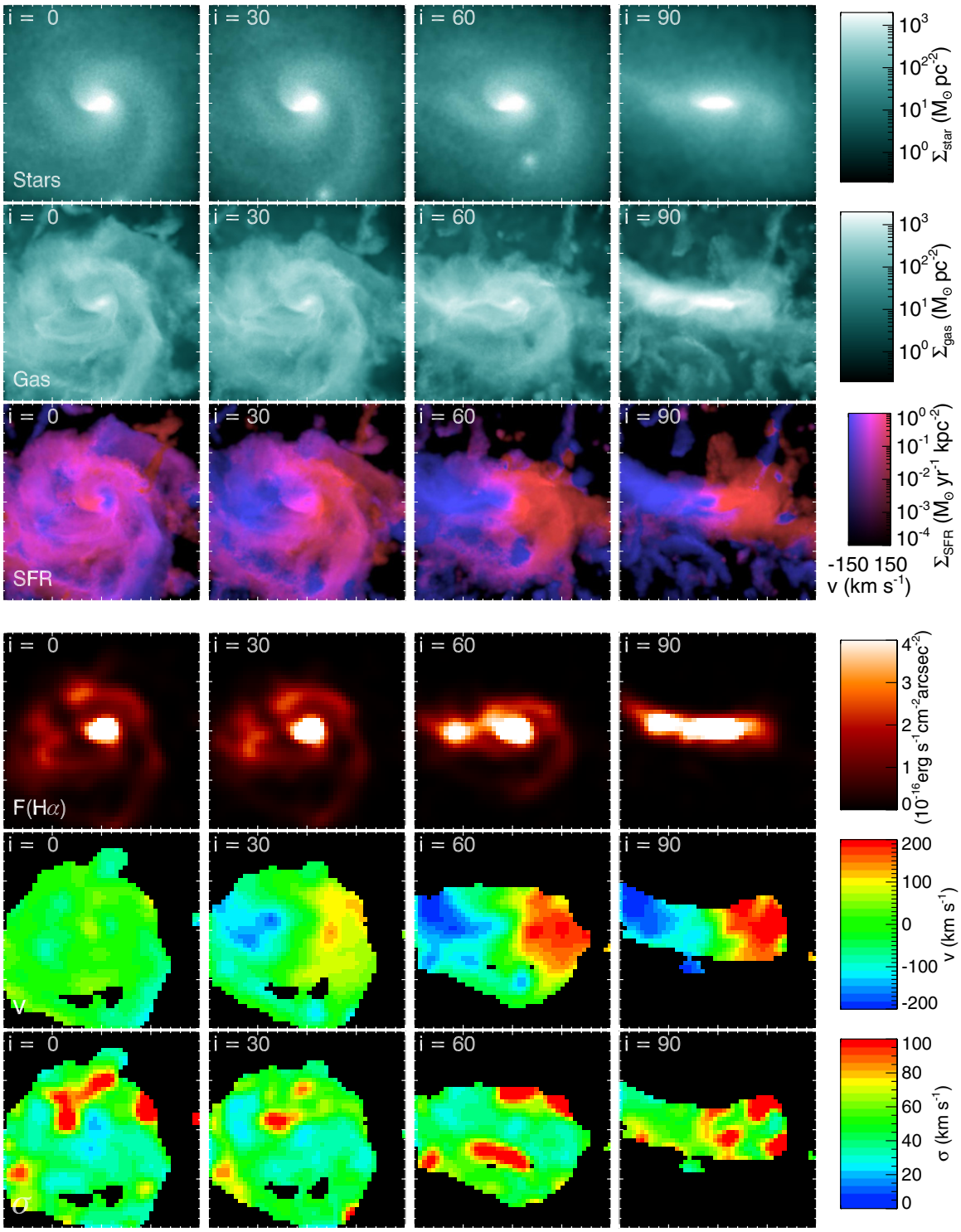

Figure 10. Same as Figure 9 for galaxy g222.
(A color version of this figure is available in the online journal.)

correlation of Daddi et al. (2007) by a factor of two to three in specific SFRs (for the vzw model), and by somewhat higher factors for the other wind models. The discrepancy is slightly worse when compared to the SINS galaxies, although the Hα selection could play some role in preferentially picking out high-SFR objects (Förster Schreiber et al. 2009). On the other hand, the difference between our simulations and the SHiZELS galaxies appears to be not as large, but note that their typical redshifts correspond to the low-z end of the redshift distribution of the SINS sample ($z \sim 1.5$), below the final redshift reached by our simulated galaxies. This discrepancy between models and data has been much debated; for instance recent *Herschel* results suggest that Hα-inferred SFRs may slightly overestimate the true (i.e., far-infrared bolometric) SFR by some non-trivial factor (Nordon et al. 2010). Other ideas for explaining this discrepancy invoke variations in the stellar initial mass function

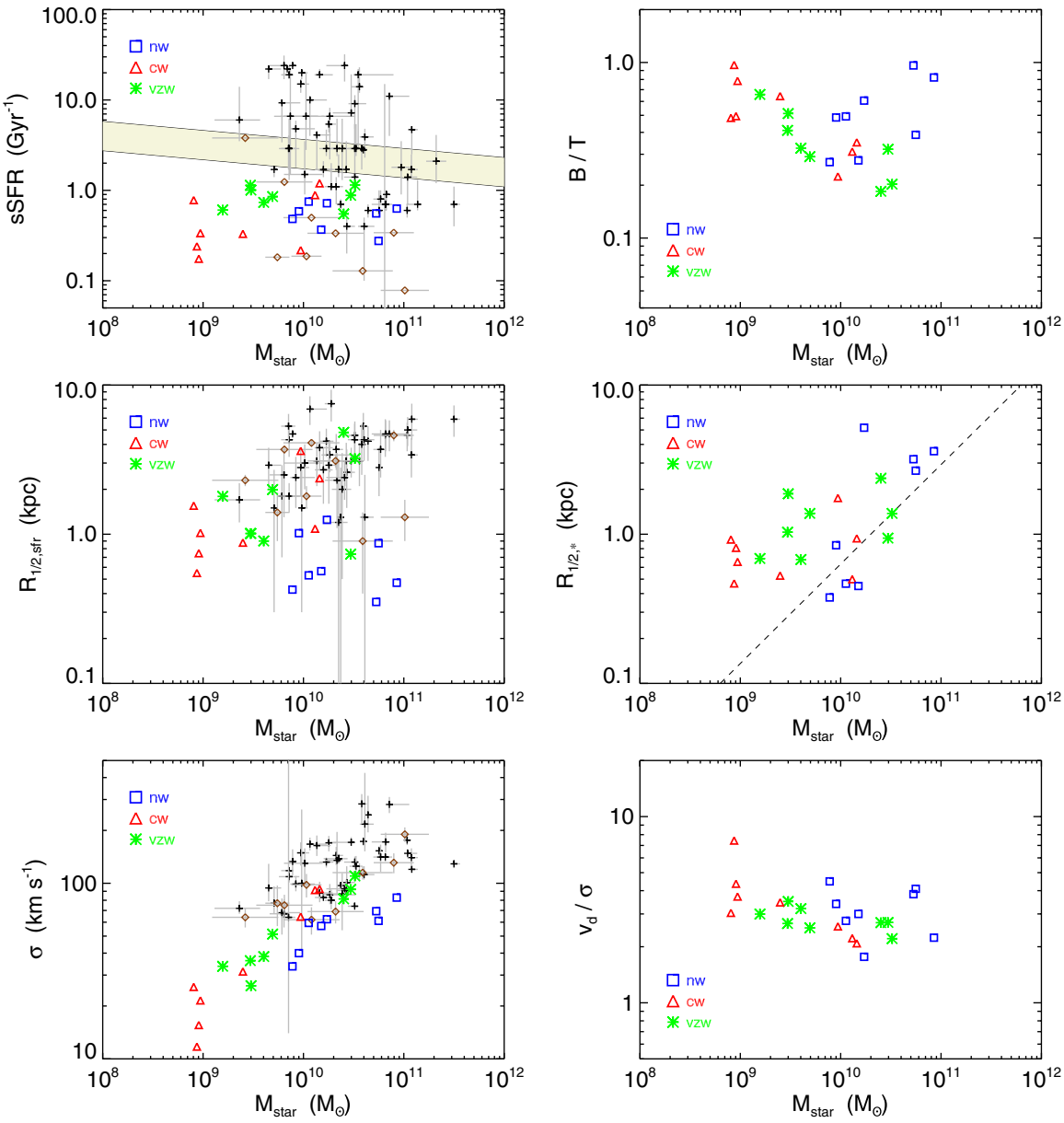

Figure 11. Structural and dynamical quantities calculated from our sample of simulated galaxies at $z = 2$, for our momentum-driven wind (vzw; green stars), constant wind (cw; red triangles), and no wind (nw; blue squares) simulations. Black crosses with grey error bars in each panel represent the $z \sim 2$ star-forming galaxies of the SINS survey (Förster Schreiber et al. 2009), while the brown diamonds correspond to a sample of galaxies from the SHiZELS survey (Swinbank et al. 2012b). Top left: specific star formation rate (sSFR) as a function of stellar mass (M_*). The shaded beige band shows the $z = 2$ $M_\star$–sSFR correlation of Daddi et al. (2007) with a scatter (semi-interquartile range) of 0.16 dex in sSFRs. Top right: stellar bulge mass fraction as a function of M_*. Middle left: radius enclosing half of the total star formation rate as a function of M_*. Middle right: radius enclosing half of the total stellar mass as a function of M_*. The dashed line shows the nominal threshold stellar surface density $M_*/R^{1.5}_{\rm half,*} = 10^{10.3}\ M_\odot\ {\rm kpc}^{-1.5}$ for compact galaxies from Barro et al. (2013). Bottom left: velocity dispersion σ of the gas component of simulated galaxies as a function of M_*. Bottom right: disk peak rotational velocity $v_{\rm d}$ divided by σ of the star-forming gas, as a function of M_* for all simulated galaxies.

(A color version of this figure is available in the online journal.)

(Narayanan & Davé 2012) or modifying the star formation law to account for metal-dependent H_2 formation (Krumholz & Dekel 2012). We will not pursue this here, except to note that our zoom simulations do not alleviate this discrepancy known from our larger cosmological runs.

Simulations with momentum-driven winds result in higher specific SFRs compared to simulations with no winds at $z = 2$, more in agreement with observations. In the vzw model, the mass loading factor scales as $\eta \sim 1/\sigma$ and outflows tend to suppress early star formation while providing high gas fractions to maintain comparatively high SFRs at later ($z \sim 2$) times, as seen in Figures 3 and 6. This suggests that even stronger outflows might be needed in simulations in order to match the $z \sim 2$ $M_\star$–SFR relation (Davé 2008). This is not trivial, however, since outflows must not be too strong lest they fail to produce enough early metals to enrich the IGM (Oppenheimer & Davé 2006, 2008) and enough photons to reionize the universe (e.g., Finlator et al. 2012).

The middle left panel of Figure 11 shows the $z = 2$ size–mass relation for all simulated galaxies. The effective radius $R_{1/2,\rm sfr}$ is defined to enclose half of the total SFR and it is calculated as a two-dimensional projected radius averaged over 100 random viewing angles. Here we see that there is a clear separation of galaxies in the $M_\star$–$R_{1/2,\rm sfr}$ plane for the different wind

models. For a given stellar mass, simulations with no winds produce galaxies with a very compact distribution of gas, with most of the star formation happening within <1 kpc from their centers. Simulations with constant winds populate the low mass and small size region of the plot, and only the more massive galaxies in the sample are able to maintain gas disks with sizes $R_{1/2,\rm sfr} > 1$ kpc. Momentum-driven winds produce more extended galaxies with sizes of several kiloparsecs, along with a minority of more compact galaxies.

Outflows affect sizes by preferentially ejecting the star-forming gas from the central regions and having it re-accrete over larger scales (Brook et al. 2012), resulting in large, extended star-forming disks that are more in agreement with SINS and SHiZELS data. Nonetheless, it is interesting that compact galaxies can also occur in the vzw case; galaxy g2403 is one such compact galaxy (see Figure 4). From our visualizations,[9] it appears that these more compact systems generally arise during or shortly after a significant merger event (Wuyts et al. 2010; Bournaud et al. 2011), but we will quantify this more rigorously in the future.

The diversity of sizes is also reflected in the half-mass radii of the stars $R_{1/2,*}$ (Figure 11, middle right). Generally, the sizes are comparable to the half-SFR radius, but in some cases $R_{1/2,*}$ can be <1 kpc. This may have interesting consequences for the progenitors of so-called compact ellipticals, i.e., early-type galaxies at $z \sim 2$ that show very high stellar densities. We show as the dashed line a nominal threshold stellar surface density of $M_*/R_{1/2,*}^{1.5} = 10^{10.3}\ M_\odot\ \mathrm{kpc}^{-1.5}$ for compact galaxies from Barro et al. (2013, see their Figure 1). The radius used for these observations is actually the *H*-band half-light radius, but this should be fairly comparable to the stellar half-mass radius. Even with winds, a small fraction of our galaxies lie above this surface density threshold (i.e., below the line). This suggests that our simulations do, with some frequency, produce galaxies that have sufficient stellar densities to be the progenitors of compact ellipticals. These simulations have no mechanism for quenching star formation, and hence our compact galaxies are still star-forming; it is an additional constraint on models to form compact passive systems that whatever feedback mechanism is responsible for quenching, it operates when the galaxy is in a dense (likely post-merger) state.

Galactic outflows seem to affect the bulge mass fraction of galaxies, as shown in Figure 11, upper right panel. To estimate the stellar bulge mass fraction, we perform a simple bulge-disk kinematic decomposition for the stellar content of all simulated galaxies. We calculate the azimuthal velocity v_ϕ of each star particle with respect to the direction of the total angular momentum of the galaxy as for our rotation curves, and estimate the bulge mass as double the mass of particles moving with $v_\phi < 0$. Though this is not analogous to observational determinations of the bulge mass, it accurately characterizes the mass in the spheroidal component of our simulated systems. With winds, the bulge fraction decreases with increasing stellar mass, suggesting that galaxies start out small and dispersion-dominated, and move toward being more ordered disks. The opposite trend is seen for our no wind simulations, tracking more the canonical behavior that galaxies start out as disks and then merge together to form more dispersion-dominated systems (e.g., White & Frenk 1991). SINS observations suggest that smaller galaxies tend to be more dispersion-dominated, qualitatively favoring our wind simulations, although a more careful comparison that accurately mimics how bulge-to-disk ratios are measured in data are needed for a more definitive result.

The lower left panel of Figure 11 shows the gas velocity dispersion, σ, as a function of stellar mass at $z = 2$. Here σ is calculated as the spatially integrated (SFR-weighted) one-dimensional velocity dispersion calculated within $R_{1/2,\rm sfr}$ and averaged over 100 random orientations. Despite being extended and rotationally supported disks, most of our galaxies are characterized by high velocity dispersions (>30 km s^{-1}). This suggests that turbulent motions are significant even in rotationally supported $z \sim 2$ galaxies, as inferred from observations (Law et al. 2009; Förster Schreiber et al. 2009; Wright et al. 2009; Swinbank et al. 2012b) and reported in previous simulations (e.g., Ceverino et al. 2010; Genel et al. 2012b). Our simulated galaxies are characterized by high σ values but still lower relative to observed $z \sim 2$ galaxies with similar stellar masses, suggesting that turbulent motions are not fully resolved at scales comparable to the spatial resolution of our simulations. Indeed, the self-regulated multi-phase model for star-forming gas is meant to capture the turbulent pressure arising from the continuous formation and disruption of gas clouds at a sub-grid level (Springel & Hernquist 2003a). For our simulated galaxies, the effective sound speed of the star-forming gas may reach values ~150 km s^{-1} (Anglés-Alcázar et al. 2013), well above the resolved large-scale turbulent velocities.

For a given stellar mass, simulations including outflows result in galaxies with higher gas velocity dispersion, in better agreement with observations. Note that since outflowing gas is hydrodynamically decoupled as it is ejected from the ISM, the outflows themselves are not directly injecting turbulence. Instead, this increased turbulence relative to simulations without winds likely owes to the higher gas and disk fractions, implying lower Toomre Q parameters for similar mass galaxies (Toomre 1964) and hence increased gravitational fragmentation, and possibly to the injection of energy due to the recycling of the outflowing gas back into the galaxies, in qualitative agreement with the analytic equilibrium model of Genel et al. (2012a).

The lower right panel of Figure 11 shows the disk rotation velocity, $v_{\rm d}$ divided by velocity dispersion σ, as a function of stellar mass. Here $v_{\rm d}$ is taken as the peak azimuthal velocity (v_ϕ) from the gas rotation curves obtained in Section 4.4. Direct comparisons with data are not straightforward since rotation is computed from a variety of means in the data, and we have not tried to mimic this in detail; hence we have not plotted data here. Nonetheless, the momentum-driven wind model yields a typical $v_{\rm d}/\sigma \sim 3$, which is in broad agreement with the turbulent high-z disks seen in SINS and SHiZELS. Constant and no wind models result in slightly higher $v_{\rm d}/\sigma$ on average, though still within the range of the data. There is little trend with mass, much less than for the stellar bulge fraction, so even though the stellar components of higher mass galaxies are diskier (for simulations with outflows), their gas content is not more rotationally supported with increasing stellar mass. Note that the stellar component is less rotationally supported than the gas in all cases (cooling of shock-heated gas may dissipate turbulent energy) and, therefore, the gas component can be rotationally supported ($v > \sigma$) even for stellar bulge-dominated galaxies. Galaxy g2743 represents an extreme example for the simulation with constant winds, with its stellar bulge fraction close to unity and still a rotationally supported gas disk (see Figures 1 and 2).

[9] See http://www.physics.arizona.edu/~angles/movies/.

Overall, the sizes and dynamical properties of simulated disks at $z = 2$ are in fair agreement with observations from the latest integral field unit studies of high-z star-forming galaxies, particularly in the case of momentum-driven winds. This occurs despite some overly simple assumptions in the modeling, such as decoupling of wind material escaping the disk, and the usual concerns about the ability of SPH to suppress viscosity and resolve dynamical instabilities (e.g., Agertz et al. 2007). Indeed, the properties of simulated galaxies are more strongly dependent on feedback models relative to the details of the specific hydrodynamic technique (e.g., Hopkins et al. 2013). This suggests that our simulations capture the dominant processes for establishing the structural properties of galaxies and provide a plausible model for the formation of disks during this cosmic epoch.

5.3. Evolution of Physical Properties

Using our plausible simulated population of $z = 2$ disk galaxies, we now examine the evolution of physical properties from $z = 8 \rightarrow 2$. We focus here on the momentum-driven wind model, since from a variety of wider constraints it is our favored model of the three presented here (see, e.g., Davé et al. 2011b, 2011a). However, many of the results are broadly similar for our other wind models. We show the evolutionary tracks for our 8 galaxies in various colors in Figure 12. Since we are interested on the evolution of galaxies on cosmological timescales, all physical quantities have been averaged over time intervals of ∼150 Myr. All tracks go from left to right (i.e., lower to higher mass), with individual unit redshifts indicated by the points along the tracks starting at $z = 8$. The same data as shown in Figure 11 is reproduced here, but note that this is for observed $z \approx 2$ galaxies and hence it is shown here for reference.

The top left panel of Figure 12 shows the evolutionary tracks of simulated galaxies in the main sequence (M_*–sSFR) plane. All galaxies show a similar evolution of decreasing specific SFR as they increase their stellar mass, consistent with a roughly linear SFR to M_* relation with the overall normalization decreasing with redshift. Despite the increase in stellar mass, mergers cause a temporary enhancement of specific SFRs relative to the dominant decreasing trend. These variations in specific SFR are apparent in the evolutionary tracks of our simulated galaxies even after averaging over time intervals of ∼150 Myr. For the three most massive galaxies—g222 (blue), g2403 (green), and g54 (red)—major mergers can be identified in Figure 3 as abrupt changes in their stellar mass, and connected to the effects on the evolutionary tracks in Figure 12 by direct comparison to the location of the points indicating integer redshifts.

At $z = 2$, galaxy sizes scale with stellar mass for simulations with winds, in agreement with observations (Figure 11). Middle panels in Figure 12 show that galaxies tend to increase in size with time, as expected, but their evolutionary tracks exhibit significant variation between galaxies, resulting in a large scatter in the size–mass diagram at any given redshift. Large variations of the half-SFR radius, $R_{1/2,\mathrm{sfr}}$, tend to occur in redshift intervals during which a major galaxy merger is taking place. This suggests that major mergers, despite representing only a fraction of the total mass growth in galaxies (e.g., Kereš et al. 2005; Rodighiero et al. 2011), have a significant impact on galaxy sizes, as it appears from our visualizations. The evolution of the stellar half-mass radius, $R_{1/2,*}$, roughly follows that of the star-forming gas and is also imprinted by significant variations occurring during galaxy mergers. Interestingly, our most compact galaxy at $z = 2$ (g2403; green evolutionary track) was also in the compact regime at $z \sim 4$, both cases preceded by a major merger (see Figure 3, middle panel). This suggests that major mergers may drive galaxies toward the region of the size–mass diagram populated by compact ellipticals. At the earliest epochs, the radius of galaxies does not change much, and may in fact become smaller with time. This partly reflects our star formation criterion of $n_H > 0.13\ \mathrm{cm}^{-3}$ that results in star formation occurring over a wide area when the universe is very dense; it is therefore unlikely to be a robust prediction.

The upper right panel of Figure 12 shows the stellar bulge fraction evolution. Early on, most galaxies are bulge-dominated, as a result of high merger rates and large gas reservoirs that keep the mass distribution disordered. As time proceeds, the combined effects of smooth gas accreting into galaxies with higher specific angular momentum and galactic outflows removing preferentially low angular momentum gas from their centers, cause galaxies to increase their sizes and reduce their stellar bulge fractions on average (Governato et al. 2009, 2010; Brook et al. 2011). It is interesting that this process only kicks in around $z \sim 4$ to start producing disk-dominated systems, at least for the range of galaxy masses considered here. Our simulations, thus, predict that $z \sim 4$ was the beginning of the epoch of disk formation for massive galaxies. By $z \sim 2$, this results in a trend of decreasing bulge fraction with increasing stellar mass in this wind model. We note that this trend is opposite to simple expectations from classic hierarchical galaxy formation models (e.g., White & Frenk 1991), in which disks form first and then merge later to give rise to more dispersion-dominated systems.

The bottom left panel of Figure 12 shows how simulated galaxies evolve with redshift in the M_*–σ plane. Galaxies tend to evolve along the correlation of σ and M_* observed at $z \sim 2$, extrapolated to lower masses. Disk peak rotation velocities follow a similar trend with stellar mass, giving rise to a nearly constant ratio $v_\mathrm{d}/\sigma \approx 3$ for all simulated galaxies independent of redshift, as shown in Figure 12, bottom right panel. Hence while the predicted v_d/σ values are similar to that observed at $z = 2$, it remains to be seen whether these same simulations can produce very thin disks as seen at $z = 0$. In order to do so, something must alter the current evolution of v_d/σ, perhaps as a result of the dropping accretion rate or else the dropping outflow rate. Note that the simulated velocity dispersions shown here have been averaged over many random directions, in analogy with the spatially integrated σ values uncorrected for average background velocity gradients inferred for the SINS galaxies (Förster Schreiber et al. 2009). Contributions from disk rotation velocities may thus overestimate σ values and underestimate the inferred rotational support of galaxies. For simulated galaxies, we can eliminate the contributions from ordered rotation simply by calculating the velocity dispersion along the line of sight perpendicular to the plane of the disk, σ_z. Interestingly, while we find $\sigma_z < \sigma$ in most cases, as expected, σ_z is also correlated with the stellar mass of galaxies.

Overall, the redshift evolution of these properties shows a consistent buildup of size and velocity dispersion with time (and mass), although mergers can particularly impact the inferred sizes substantially over short time periods. The large scatter in observed sizes may, therefore, reflect the short-term merger history of galaxies even more reliably than instantaneous SFRs or bulge-to-disk ratios. Galaxies evolve from being bulge-dominated when small to disk-dominated when larger, with disks becoming prominent only at $z \lesssim 4$. Despite this, galaxies

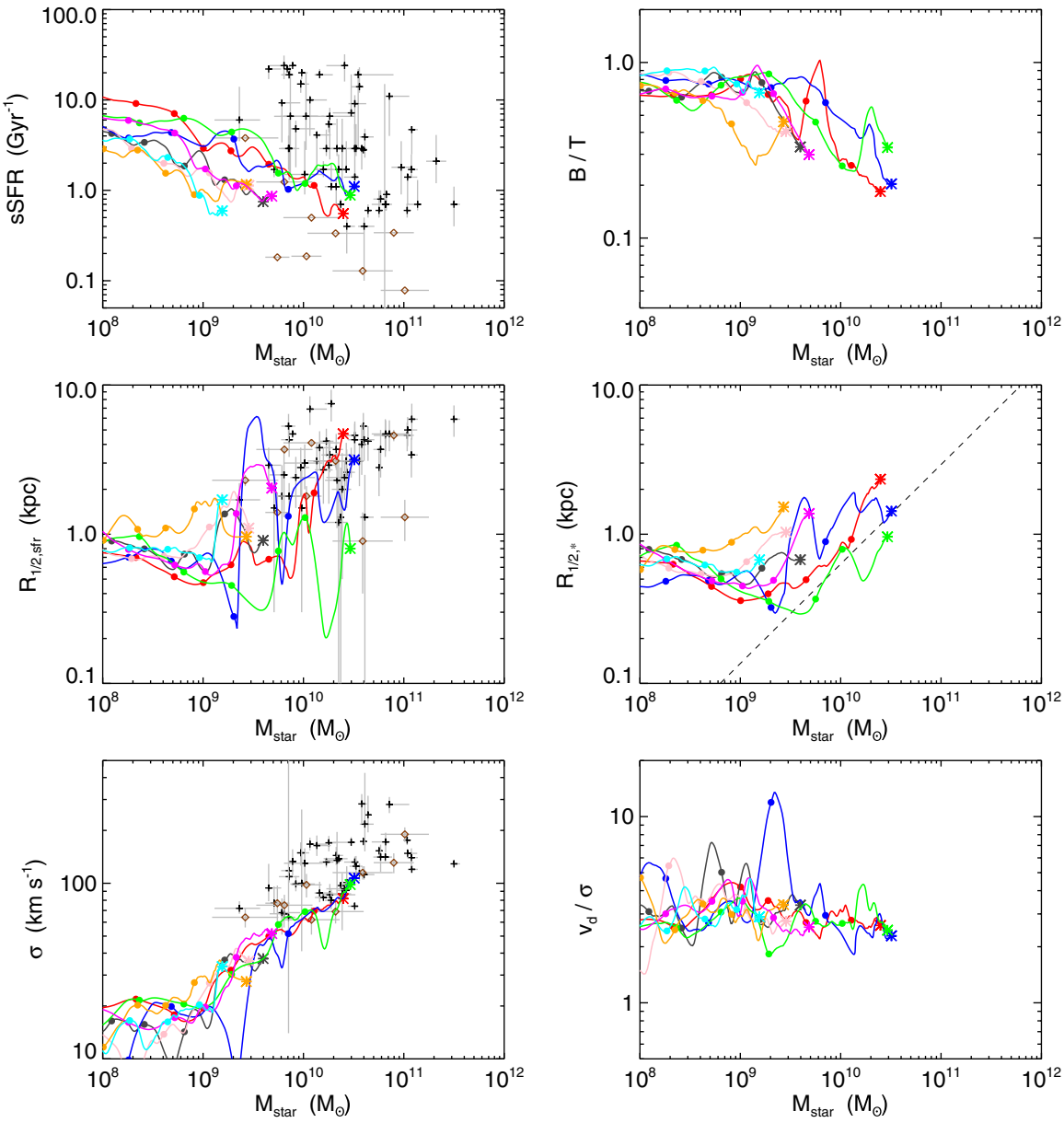

Figure 12. Evolution of structural and dynamical quantities calculated from our sample of simulated galaxies from $z = 8 \rightarrow 2$. Different color tracks show each of our eight momentum-driven wind run galaxies, with filled circles indicated at integer redshifts (stars show the location of galaxies at the end of the simulation at $z = 2$). Other lines and symbols are as in Figure 11. Top left: specific star formation rate (sSFR) as a function of stellar mass (M_*). Top right: stellar bulge mass fraction as a function of M_*. Middle left: radius enclosing half of the total star formation rate as a function of M_*. Middle right: radius enclosing half of the total stellar mass as a function of M_*. Bottom left: velocity dispersion σ of the gas component of simulated galaxies as a function of M_*. Bottom right: disk peak rotational velocity v_d divided by σ of the star-forming gas, as a function of M_* for all simulated galaxies. The time evolution of all physical quantities has been averaged over time intervals of ∼150 Myr.

(A color version of this figure is available in the online journal.)

are always rotationally supported even at early times when bulge-dominated, suggesting that the present-day association between small bulge-to-disk ratio and large rotational support does not necessarily apply to high-redshift galaxies.

6. RESOLUTION CONVERGENCE

A key computational issue we face in this study is that the spatial resolution of the observations we are comparing our results against is comparable to the numerical resolution of our simulations. Our nominal ∼220 pc resolution at $z = 2$ corresponds to the equivalent Plummer force softening length; thus, the scale at which we compute exact gravitational forces is 2.8 times this length, or ∼600 pc. Furthermore, SPH techniques may suffer from large viscous transport of angular momentum. Indeed, the moving mesh code Arepo (Springel 2010) is seen to produce larger-scale disks than Gadget (Vogelsberger et al. 2012; Torrey et al. 2012) from identical initial conditions. Other recent code comparisons suggest that differences in sub-grid physics may have an even stronger impact on the properties of simulated galaxies relative to differences in hydrodynamic techniques (Scannapieco et al. 2012; Hopkins 2013; Hopkins et al. 2013). It is, therefore, important to carry out a basic test of resolution convergence of our key results.

We run simulations with a factor of two lower spatial resolution and a factor of eight lower mass resolution, equivalent to

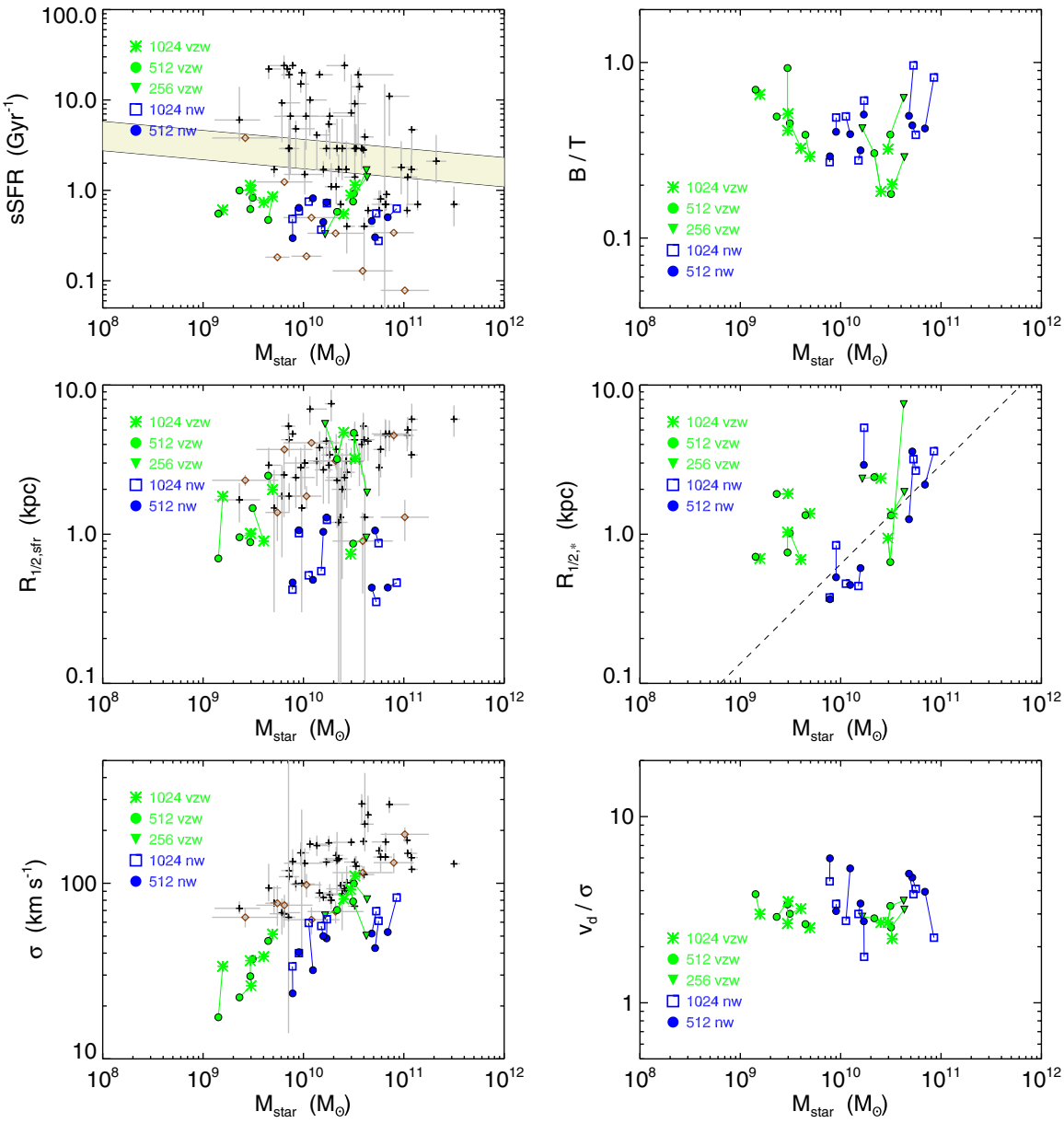

Figure 13. Resolution convergence of physical quantities at $z = 2$ for our momentum-driven wind (vzw; green) and no wind (nw; blue) simulations, comparing our effective 1024^3 runs (green stars and blue squares for vzw and nw respectively) with effective 512^3 runs (green and blue filled circles for vzw and nw respectively) of the same initial conditions. Green and blue solid lines connect individual galaxies corresponding to the higher resolution and lower resolution simulations for the vzw and nw simulations respectively. The green triangles show the physical properties of the three most massive galaxies as obtained from the original large-scale 256^3 simulation with momentum-driven winds. Other lines and symbols are as in Figure 11. Top left: specific star formation rate (sSFR) as a function of stellar mass (M_*). Top right: stellar bulge mass fraction as a function of M_*. Middle left: radius enclosing half of the total star formation rate as a function of M_*. Middle right: radius enclosing half of the total stellar mass as a function of M_*. Bottom left: velocity dispersion σ of the gas component of simulated galaxies as a function of M_*. Bottom right: disk peak rotational velocity v_d divided by σ of the star-forming gas, as a function of M_* for all simulated galaxies.

(A color version of this figure is available in the online journal.)

512^3 resolution in a $[24\,h^{-1}\,\mathrm{Mpc}]^3$ box, from otherwise identical initial conditions, and identify the galaxies that correspond to our high-resolution galaxy sample. In addition, we extend our resolution study by using the original large-scale cosmological simulation with momentum-driven winds and 256^3 resolution. The unique identification of galaxies corresponding to our highest resolution galaxy sample is increasingly difficult as the resolution decreases and galaxy trajectories begin to differ. Nonetheless, we have been able to identify and calculate the properties of our three most massive galaxies, extending the resolution study over 64 times in mass and 4 times in spatial scale.

Figure 13 shows the effects of numerical resolution on key structural and dynamical quantities of galaxies versus stellar mass for our momentum-driven winds and no wind simulations at $z = 2$ (as in Figure 11). Here, solid lines (green and blue for vzw and nw respectively) connect individual galaxies corresponding to the higher and lower resolution simulations to help identify any systematic trends. We note that a galaxy-by-galaxy comparison represents a strong numerical convergence test given that even small deviations of orbital parameters in galaxy mergers may result in rather different structural and kinematic properties of remnant galaxies at a given time.

Global properties of galaxies are thus expected to exhibit better numerical convergence. Indeed, Figure 13 shows that total stellar masses and specific SFRs of galaxies are both well converged for the vzw and nw simulations. The average ratios $\langle \mathrm{sSFR}_{512}/\mathrm{sSFR}_{1024} \rangle$ and $\langle M_{*,512}/M_{*,1024} \rangle$ are consistent with unity within the 1σ dispersion when comparing the effective 512^3 and 1024^3 simulations.

The size of galaxies is somewhat more sensitive to resolution, as shown in Figure 13, middle panels. For individual galaxies, we find that the half-SFR ($R_{1/2,\mathrm{sfr}}$) and half-mass ($R_{1/2,*}$) radii may differ by up to a factor of $\sim$2 for the effective 1024^3, 512^3, and 256^3 simulations at $z = 2$. Such sensitivity might be expected given that radii track recent merger activity, which can vary substantially owing to the chaotic nature of orbits within hierarchically growing halos. Indeed, the most compact galaxy in the sample is in the early stages of a major merger with a gas poor galaxy at $z = 2$ in our 256^3 simulation, resulting in a strong variation in stellar effective radius without significantly affecting $R_{1/2,\mathrm{sfr}}$. Despite this, we find no systematic trend in the whole sample with resolution or wind model—the average size ratio $\langle R_{512}/R_{1024} \rangle$ is consistent with no resolution dependence for both the stellar and gas distributions. Our lower resolution simulations confirm that outflows generally produce more extended star-forming disk galaxies but that may also result in compact galaxies (similar to simulations with no winds) with some frequency.

Stellar bulge mass fractions are also somewhat sensitive to resolution, as shown in the upper right panel of Figure 13. In the vzw case, bulge fractions are generally higher at low resolution. This is expected if the lack of gravitational resolution results in increased random motions and the overall reduction of ordered rotation due to a comparatively shallower gravitational potential. Such a trend is not as apparent in the no wind case, though in two cases the bulge fractions are substantially different. Overall, our general result that bulge fractions are higher for similar mass galaxies in simulations with no winds seems unaffected by resolution.

We find a systematic trend for gas velocity dispersion (σ) to decrease with resolution (Figure 13, lower left), though this is significantly more evident for simulations without winds. This suggests that our effective 1024^3 simulations may not have reached numerical convergence and that higher resolution simulations with outflows could result in slightly higher σ values for a given stellar mass, more in agreement with observations. Despite this, gas recycling for simulations with outflows seems to result in increasing σ values and, therefore, turbulence in galaxies regardless of numerical resolution. Figure 13, lower right, shows that the ratio v_d/σ is reasonably well converged for the vzw model but increases systematically for nw simulations with lower resolution due to the overall decrease in σ.

In short, our main results are generally though not optimally resolution converged. Higher resolution seems to result in lower stellar bulge fractions and higher gas velocity dispersions, while we find no systematic trend for galaxy sizes with resolution. However, the resolution convergence exhibited by the wind simulations is better than that for no winds. Interestingly, this trend is also seen for global mass and SFR functions (Davé et al. 2011b). By increasing sizes and having a physically motivated driver of wind recycling that sets the velocity dispersion, winds actually seem to help resolution convergence somewhat. Nonetheless, this convergence experiment only spanned a factor of 4 in spatial scale and 64 in mass (for our three most massive galaxies), and hence simulations with greater dynamic range will be needed to fully assess the numerical robustness of these results.

7. SUMMARY AND CONCLUSIONS

Powerful galactic outflows are ubiquitous in high-redshift galaxies and likely play a central role in the evolution of galaxies and the IGM. Here, we have presented high-resolution cosmological zoom simulations that follow the evolution of a sample of eight central galaxies down to $z = 2$, focusing on the impact of strong outflows on their morphologies, kinematics, and star formation properties. Our main results can be summarized as follows:

1. Despite the limited sample of eight galaxies presented here, our simulated systems span a wide range of morphological characteristics at $z = 2$. Disk structures are prevalent but can range from very compact gas and stellar distributions, to extended quiescent "grand-design" spirals, to turbulent and clumpy disks. Inferred morphologies can depend on the observed tracer.
2. Simulations with no winds produce rapidly rising SFRs that result in higher stellar masses, higher metallicities, and lower gas fractions for all galaxies at all times relative to simulations with galactic outflows. Momentum-driven winds cause an effective delay in star formation by ejecting significant amounts of gas from small, early galaxies and having it reaccreted at later times, resulting in higher gas fractions and star formation histories more in agreement with observations. All wind models fail, however, in reproducing the normalization of the observed $z = 2$ $M_\star$–SFR relation, though the late-time recycling by the momentum-driven wind model comes the closest; this suggests that even stronger outflows at early times and/or small masses may be required.
3. Galactic outflows affect the amount and distribution of metals in galaxies by regulating star formation, ejecting metals into the surrounding gas preferentially from their centers, and the recycling of enriched gas back into galaxies over larger scales. This results in lower metallicities and less steep metallicity gradients relative to simulations with no winds. The resulting central metallicities are somewhat super-solar. Examples of inverted metallicity gradients are uncommon among our galaxy sample.
4. Winds have a significant impact on the structural properties of simulated galaxies. No wind simulations generally produce more compact galaxies with higher stellar surface densities, higher stellar mass bulge fractions, and most of the star-forming gas concentrated within the inner kiloparsec. Galactic winds usually yield more extended disks and tend to reduce bulge fractions by preferentially removing low angular momentum gas from their centers. Nonetheless, simulations with winds may produce, in some cases, galaxies with stellar surface densities above the threshold for compact ellipticals, usually occurring shortly after a major merger event. Sizes in general are quite sensitive to the merger history, more so than star formation or bulge fraction, and hence this may be the best way to assess the hierarchical buildup of galaxies.
5. Simulations with winds produce galaxies with more gradually rising rotation curves compared to the more centrally peaked rotation curves of galaxies without winds. When calculated from the gas rotation velocities rather than the

enclosed mass, rotation curves are more smoothly rising because of the increased dispersion support in the central regions of galaxies.

6. Peak rotation velocities and velocity dispersions scale with stellar mass for all wind models, in a manner broadly consistent with observations. The inferred ratios v_d/σ are consistent with rotationally supported turbulent disks at $z = 2$. Gas recycling and the high gas fractions of galaxies from simulations with outflows yield higher gas velocity dispersions and more turbulent disks compared to no-wind simulations. Early small galaxies have both high bulge fraction and are rotation-dominated, counter to typical trends among local galaxies, and suggests that the standard intuition from today's Hubble sequence may not apply to high-z galaxies.

Our simulations complement previous studies by analyzing the effects of large-scale outflows on the internal structure and evolution of individual $z = 2$ galaxies. We employ the same outflow mechanisms used by Davé et al. (2011b, 2011a) in non-zoom cosmological simulations, including an observationally constrained prescription for momentum-driven winds, and with no further tuning of model parameters. Encouragingly, simulations with momentum-driven winds, which are favored by a wide range of observations and recent idealized galaxy simulations (Hopkins et al. 2012), yield similar trends on the global properties of galaxies when applied to simulations with a factor $\times 150$ increased in mass resolution, and produce galaxies at $z = 2$ with structural and kinematic properties in broad agreement with observations. This provides a new and non-trivial test of hierarchical galaxy formation models.

It is interesting that even among our limited galaxy sample, we produce a diversity of morphologies, from grand design spirals to clumpy turbulent disks to potential progenitors of compact ellipticals. This diversity is enhanced by feedback, and may in fact be governed by it. While there is an overall consensus on the importance of feedback associated with star formation in determining the morphologies of galaxies and their evolution over cosmic time, major uncertainties remain on the nature and relative significance of different feedback processes. The specific outcomes of particular feedback models often depend on numerical resolution, the treatment of ISM physics, the star formation prescription, and other implementation details (Ceverino et al. 2010; Governato et al. 2010; Krumholz & Dekel 2012; Scannapieco et al. 2012; Christensen et al. 2012; Hopkins et al. 2012).

Generically, we find that increasing the strength of feedback results in the reduction of star formation efficiencies and the increase in galaxy sizes for a given stellar mass, as found in, e.g., Sales et al. (2010). Galactic outflows also increase the degree of rotational support of galaxies by preferentially removing low angular momentum gas from their centers (Governato et al. 2010; Brook et al. 2011, 2012). Disk galaxies may survive or even be produced from high angular momentum mergers of gas-rich systems, provided that pressurization from a multiphase ISM prevents fragmentation and efficient conversion of gas into stars (Robertson et al. 2004, 2006; Hopkins et al. 2009a, 2009b). Simulations with no thermally pressurized ISM, however, tend to produce more turbulent and clumpy disks and may result in rather different merger remnant morphologies (Bournaud et al. 2011). These illustrate how the structure and morphology of high-redshift galaxies provide yet another important test of feedback processes during the peak epoch of galaxy growth.

The progress of high performance computing has enabled these types of cosmological zoom simulations to become more routine, but they still rely on sub-grid prescriptions and are subject to numerical uncertainties. Advancing this field will rely on developing more robust models for the small-scale physics in addition to achieving higher dynamic range. This work presents a first step toward developing plausible models for the formation of galactic systems down to sub-kiloparsec scales, but much work lies ahead to push both to smaller scales and to understand better the underlying physical processes governing high-redshift galaxy assembly.

We thank D. Ceverino, C. Christensen, C. Martin, B. Robertson, and G. Yepes for useful discussions, and the anonymous referee for a thoughtful report that helped improve the paper. D.A.-A. thanks B. Robertson for very useful assistance with data visualization. F.Ö. gratefully acknowledges support from the Radcliffe Institute for Advanced Study at Harvard University. The simulations were run on the University of Arizona's 512-processor SGI Altix system and the TACC Sun Constellation Cluster (Ranger) at The University of Texas, Austin. This work used the Extreme Science and Engineering Discovery Environment (XSEDE), which is supported by National Science Foundation grant number OCI-1053575. This work was supported by the National Science Foundation under grant numbers AST-0907998 and AST-1108753. Computing resources were obtained through grant number DMS-0619881 from the National Science Foundation.

REFERENCES

Agertz, O., Moore, B., Stadel, J., et al. 2007, MNRAS, 380, 963
Alaghband-Zadeh, S., Chapman, S. C., Swinbank, A. M., et al. 2012, MNRAS, 424, 2232
Anglés-Alcázar, D., Özel, F., & Davé, R. 2013, ApJ, 770, 5
Barai, P., Viel, M., Borgani, S., et al. 2013, MNRAS, 430, 3213
Barro, G., Faber, S. M., Pérez-González, P. G., et al. 2013, ApJ, 765, 104
Bournaud, F., Chapon, D., Teyssier, R., et al. 2011, ApJ, 730, 4
Brook, C. B. 2011, MNRAS, 415, 1051
Brook, C. B., Stinson, G., Gibson, B. K., et al. 2012, MNRAS, 419, 771
Ceverino, D., Dekel, A., & Bournaud, F. 2010, MNRAS, 404, 2151
Chabrier, G. 2003, PASP, 115, 763
Chapman, S. C., Ivison, R. J., Roseboom, I. G., et al. 2010, MNRAS, 409, L13
Christensen, C., Governato, F., Quinn, T., et al. 2012, arXiv:1211.0326
Cresci, G., Hicks, E. K. S., Genzel, R., et al. 2009, ApJ, 697, 115
Cresci, G., Mannucci, F., Maiolino, R., et al. 2010, Natur, 467, 811
Daddi, E., Dickinson, M., Morrison, G., et al. 2007, ApJ, 670, 156
Davé, R. 2008, MNRAS, 385, 147
Davé, R., Finlator, K., & Oppenheimer, B. D. 2006, MNRAS, 370, 273
Davé, R., Finlator, K., Oppenheimer, B. D., et al. 2010, MNRAS, 404, 1355
Davé, R., Finlator, K., & Oppenheimer, B. D. 2011a, MNRAS, 416, 1354
Davé, R., Finlator, K., & Oppenheimer, B. D. 2012, MNRAS, 421, 98
Davé, R., Oppenheimer, B. D., & Finlator, K. 2011b, MNRAS, 415, 11
Dekel, A., Birnboim, Y., Engel, G., et al. 2009, Natur, 457, 451
Dekel, A., & Krumholz, M. R. 2013, MNRAS, 432, 455
Elbaz, D., Daddi, E., Le Borgne, D., et al. 2007, A&A, 468, 33
Elmegreen, B. G., Elmegreen, D. M., Fernandez, M. X., & Lemonias, J. J. 2009, ApJ, 692, 12
Elmegreen, D. M., Elmegreen, B. G., & Hirst, A. C. 2004, ApJL, 604, L21
Finlator, K., & Davé, R. 2008, MNRAS, 385, 2181
Finlator, K., Davé, R., & Oppenheimer, B. D. 2007, MNRAS, 376, 1861
Finlator, K., Davé, R., Papovich, C., & Hernquist, L. 2006, ApJ, 639, 672
Finlator, K., Oh, S. P., Özel, F., & Davé, R. 2012, MNRAS, 427, 2464
Förster Schreiber, N. M., Genzel, R., Bouché, N., et al. 2009, ApJ, 706, 1364
Förster Schreiber, N. M., Genzel, R., Lehnert, M. D., et al. 2006, ApJ, 645, 1062
Förster Schreiber, N. M., Shapley, A. E., Genzel, R., et al. 2011, ApJ, 739, 45
Geach, J. E., Smail, I., Best, P. N., et al. 2008, MNRAS, 388, 1473
Genel, S., Dekel, A., & Cacciato, M. 2012a, MNRAS, 425, 788
Genel, S., Naab, T., Genzel, R., et al. 2012b, ApJ, 745, 11
Genzel, R., Newman, S., Jones, T., et al. 2011, ApJ, 733, 101

Governato, F., Brook, C. B., Brooks, A. M., et al. 2009, MNRAS, 398, 312
Governato, F., Brook, C., Mayer, L., et al. 2010, Natur, 463, 203
Haardt, F., & Madau, P. 2001, in Clusters of Galaxies and the High Redshift Universe Observed in X-Rays, ed. D. M. Neumann & J. T. T. Van (CEA Saclay), 64
Hinshaw, G., Larson, D., Komatsu, E., et al. 2013, ApJS, 208, 19
Hirschmann, M., Naab, T., Davé, R., et al. 2013, MNRAS, 436, 2929
Hopkins, A. M., & Beacom, J. F. 2006, ApJ, 651, 142
Hopkins, P. F. 2013, MNRAS, 428, 2840
Hopkins, P. F., Cox, T. J., Younger, J. D., & Hernquist, L. 2009a, ApJ, 691, 1168
Hopkins, P. F., Keres, D., Oñorbe, J., et al. 2013, arXiv:1311.2073
Hopkins, P. F., Somerville, R. S., Cox, T. J., et al. 2009b, MNRAS, 397, 802
Hopkins, P. F., Quataert, E., & Murray, N. 2012, MNRAS, 421, 3522
Jones, T., Ellis, R. S., Richard, J., & Jullo, E. 2013, ApJ, 765, 48
Kannan, R., Stinson, G. S., Macciò, A. V., et al. 2013, MNRAS
Kartaltepe, J. S., Dickinson, M., Alexander, D. M., et al. 2012, ApJ, 757, 23
Katz, N., Weinberg, D. H., & Hernquist, L. 1996, ApJS, 105, 19
Kennicutt, R. C. 1998a, ApJ, 498, 541
Kennicutt, R. C. 1998b, ARA&A, 36, 189
Kereš, D., Katz, N., Weinberg, D. H., & Davé, R. 2005, MNRAS, 363, 2
Kitayama, T., & Suto, Y. 1996, ApJ, 469, 480
Komatsu, E., Dunkley, J., Nolta, M. R., et al. 2009, ApJS, 180, 330
Kornei, K. A., Shapley, A. E., Martin, C. L., et al. 2012, ApJ, 758, 135
Krumholz, M. R., & Dekel, A. 2012, ApJ, 753, 16
Krumholz, M. R., & Thompson, T. A. 2013, MNRAS, 434, 2329
Law, D. R., Shapley, A. E., Steidel, C. C., et al. 2012, Natur, 487, L338
Law, D. R., Steidel, C. C., Erb, D. K., et al. 2009, ApJ, 697, 2057
Lilly, S. J., Carollo, C. M., Pipino, A., Renzini, A., & Peng, Y. 2013, ApJ, 772, 119
Madau, P., Ferguson, H. C., Dickinson, M. E., et al. 1996, MNRAS, 283, 1388
Martin, C. L. 2005, ApJ, 621, 227
Martin, C. L., Shapley, A. E., Coil, A. L., et al. 2012, ApJ, 760, 127
McCarthy, I. G., Schaye, J., Font, A. S., et al. 2012, MNRAS, 427, 379
McKee, C. F., & Ostriker, J. P. 1977, ApJ, 218, 148
Mo, H. J., Mau, S., & White, S. D. M. 1998, MNRAS, 295, 319
Murray, N., Quataert, E., & Thompson, T. A. 2005, ApJ, 618, 569
Murray, N., Quataert, E., & Thompson, T. A. 2010, ApJ, 709, 191
Narayanan, D., & Davé, R. 2012, MNRAS, 423, 3601
Navarro, J. F., & White, S. D. M. 1994, MNRAS, 267, 401
Newman, S. F., Genzel, R., Förster Schreiber, N. M., et al. 2012, ApJ, 761, 43
Noeske, K. G., Weiner, B. J., Faber, S. M., et al. 2007, ApJL, 660, L43
Nordon, R., Lutz, D., Shao, L., et al. 2010, A&A, 518, L24
Oppenheimer, B. D., & Davé, R. A. 2006, MNRAS, 373, 1265
Oppenheimer, B. D., & Davé, R. A. 2008, MNRAS, 387, 577
Oppenheimer, B. D., Davé, R., Kereš, D., et al. 2010, MNRAS, 406, 2325
Puchwein, E., & Springel, V. 2013, MNRAS, 428, 2966
Queyrel, J., Contini, T., Kissler-Patig, M., et al. 2012, A&A, 539, 93
Robertson, B., Bullock, J. S., Cox, T. J., et al. 2006, ApJ, 645, 986
Robertson, B., Yoshida, N., Springel, V., & Hernquist, L. 2004, ApJ, 606, 32
Rodighiero, G., Daddi, E., Baronchelli, I., et al. 2011, ApJL, 739, L40
Rodighiero, G., Vaccari, M., Franceschini, A., et al. 2010, A&A, 515, 8
Rupke, D. S., Veilleux, S., & Sanders, D. B. 2005, ApJS, 160, 115
Sales, L. V., Navarro, J. F., Schaye, J., et al. 2010, MNRAS, 409, 1541
Scannapieco, C., Wadepuhl, M., Parry, O. H., et al. 2012, MNRAS, 423, 1726
Schmidt, M. 1959, ApJ, 129, 243
Springel, V. 2005, MNRAS, 364, 1105
Springel, V. 2010, MNRAS, 401, 791
Springel, V., & Hernquist, L. 2002, MNRAS, 333, 649
Springel, V., & Hernquist, L. 2003a, MNRAS, 339, 289
Springel, V., & Hernquist, L. 2003b, MNRAS, 339, 312
Steidel, C. C., Erb, D. K., Shapley, A. E., et al. 2010, ApJ, 717, 289
Sutherland, R. S., & Dopita, M. A. 1993, ApJS, 88, 253
Swinbank, A. M., Smail, I., Sobral, D., et al. 2012a, ApJ, 760, 130
Swinbank, A. M., Sobral, D., Smail, I., et al. 2012b, MNRAS, 426, 935
Tacconi, L. J., Genzel, R., Neri, R., et al. 2010, Natur, 463, 781
Targett, T. A., Dunlop, J. S., Cirasuolo, M., et al. 2013, MNRAS, 432, 2012
Toomre, A. 1964, ApJ, 139, 1217
Torrey, P., Vogelsberger, M., Genel, S., et al. 2013, arXiv:1305.4931
Torrey, P., Vogelsberger, M., Sijacki, D., Springel, V., & Hernquist, L. 2012, MNRAS, 427, 2224
Troncoso, P., Maiolino, R., Sommariva, V., et al. 2013, arXiv:1311.4576
Valenzuela, O., Rhee, G., Klypin, A., et al. 2007, ApJ, 657, 773
van Dokkum, P. G., Franx, M., Kriek, M., et al. 2008, ApJL, 677, L5
Vogelsberger, M., Sijacki, D., Kereš, D., Springel, V., & Hernquist, L. 2012, MNRAS, 425, 3024
Weiner, B. J., Coil, A. L., Prochaska, J. X., et al. 2009, ApJ, 692, 187
Weinmann, S. M., Pasquali, A., Oppenheimer, B. D., et al. 2012, MNRAS, 426, 2797
White, S. D. M., & Frenk, C. S. 1991, ApJ, 379, 52
Wright, S. A., Larkin, J. E., Law, D. R., et al. 2009, ApJ, 699, 421
Wuyts, S., Cox, T. J., Hayward, C. C., et al. 2010, ApJ, 722, 1666
Wuyts, S., Förster Schreiber, N. M., Genzel, R., et al. 2012, ApJ, 753, 114
Wuyts, S., Förster Schreiber, N. M., Lutz, D., et al. 2011, ApJ, 738, 106
Yuan, T.-T., Kewley, L. J., Swinbank, A. M., Richard, J., & Livermore, R. C. 2011, ApJL, 732, L14